

VOLCANO INFRASOUND MONITORING WITH APPLICATIONS  
FOR STATISTICAL FORECASTING OF EXPLOSIONS AT  
SAKURAJIMA (JAPAN)

by  
Matthew R. VonLintig

A thesis  
submitted in partial fulfillment  
of the requirements for the degree of  
Master of Science in Geophysics  
Boise State University

December 2018

© 2018

Matthew R. VonLintig

ALL RIGHTS RESERVED

BOISE STATE UNIVERSITY GRADUATE COLLEGE

**DEFENSE COMMITTEE AND FINAL READING APPROVALS**

of the thesis submitted by

Matthew R. VonLintig

Thesis Title: Volcano Infrasound Monitoring with Applications for Statistical Forecasting of Explosions at Sakurajima (Japan)

Date of Final Oral Examination: 20 July 2018

The following individuals read and discussed the thesis submitted by student Matthew R. VonLintig, and they evaluated the students presentation and response to questions during the final oral examination. They found that the student passed the final oral examination.

Jeffrey B Johnson Ph.D.

Chair, Supervisory Committee

John R (Jack) Pelton Ph.D.

Member, Supervisory Committee

Jodi Mead Ph.D.

Member, Supervisory Committee

The final reading approval of the thesis was granted by Jeffrey B Johnson Ph.D., Chair of the Supervisory Committee. The thesis was approved by the Graduate College.

## ACKNOWLEDGMENT

Although I am the sole author of this thesis document, I must acknowledge those who helped to cultivate, seed, water, talk to, nurture, and harvest this fruit:

My fearless advisor, Jeff, who showed no sign of fear when taking me on as a grad student; if Jeff hadn't gave me the idea of continuing my education in geophysics I surely would not be where I am right now.

My committee members, both official and otherwise, for relating to me as a graduate student by sharing stories and experiences, for getting excited about my research and giving me opportunities to push myself, and for providing me with essential feedback that will help me grow as a scientist, speaker, writer, and person.

My friend, colleague, and cubicle-mate Tate, for entertaining my imagination with chats about giant squid, black holes, and  $\sqrt{2}$ ; and for raising the bar, helping lift me towards that bar, and walking back to the office after a couple beers at the bar.

My grandmother, Wilma, for sharing with me her passion for knowledge, her excitement and curiosity, and her love for life.

My parents, Bob and Stephanie, for their unconditional love and support for the past 26.386111 years.

My older brother, Mike, for expanding my forward view on life by clearing low-hanging branches that obscure vision through blazing a trail of his own.

The Geophysics Club, for engaging in community activities and putting in their

blood, sweat, and time (no tears) in pursuit of answers.

The people who I saw every day in the ERB, for being friendly faces and a positive influence on myself and my studies.

And you, for re-igniting my inspiration and childishness just as I found myself getting complacent; and for being 'not just anybody'.

## AUTOBIOGRAPHICAL SKETCH



Science is art.

## ABSTRACT

Volcanic eruptions are powerful natural phenomena that often occur unpredictably in time and magnitude. Nearby communities are put at risk during volcanic unrest; however, when hazards are well understood and clearly defined risk can be mitigated. This thesis addresses the problem of forecasting the likelihood of future explosive volcanic behavior by monitoring ongoing eruptive history with infrasound. I parameterize inter-event temporal behavior to distinguish between the eruption controlling processes of material failure rate and magma and volatile supply.

I analyze data from Sakurajima, a type-example open volcano, using two local (4 km from the vent) microphone arrays, which recorded infrasound continuously from 18-25 July 2013. Both explosive and emergent degassing events are classified using the infrasound data, along with the inter-eruptive quiescent periods. I use the Fisher statistic to quantitatively measure acoustic signal coherency originating from Sakurajimas active vent, Showa crater. This allows me to determine the statistics associated with vent activity prior to 366 detected degassing events. All observed 366 repose intervals form a distribution that I compare with known exponential, gamma, and Weibull probability distribution models. The entire set of repose interval lengths is best fit by a gamma distribution model representative of a stationary Poisson process, suggesting that events are controlled by material failure phenomenon rather than a dynamic process such as changes in magma or volatile flux.

Detected volcano infrasound is categorized based on recorded pressure amplitude as either explosive ( $> 3.5$  Pa) or passive degassing ( $< 3.5$  Pa). By observing the separate distributions of repose interval lengths that precede the two eruptive modes, I develop a forecasting variable, the Relative Squared Median Residual Sum (RSMRS) that describes which mode is more likely to occur during an observed period of quiescence, based on past behavior. The forecasting reliability depends on the separation and the peakedness of RSMRS distributions for each mode. A RSMRS threshold value is used to anticipate either passive degassing or explosive degassing. Results may differ for other volcanoes with different styles of eruption or for Sakurajima activity during different periods.

The RSMRS forecaster is run coincident with signal detection and is capable of operation in near real-time with the availability of telemetered data. The forecasting algorithm is trained with enough data such that repose interval distribution for each mode of activity begins to take shape. Consistent with Poisson process (gamma distribution) assumptions, each eruptive mode converges on its respective arrival rate. Explosion forecasting results in 76% true positive (anticipated explosion resulted in explosion) rate at an RSMRS cutoff of 0.2998. The true negative rate was 97.5% and is defined as correctly anticipating passive degassing following periods of quiescence.

# TABLE OF CONTENTS

ACKNOWLEDGMENT . . . . .	iv
AUTOBIOGRAPHICAL SKETCH . . . . .	vi
ABSTRACT . . . . .	vii
LIST OF TABLES . . . . .	xi
LIST OF FIGURES . . . . .	xii
LIST OF VARIABLES . . . . .	xviii
LIST OF ABBREVIATIONS . . . . .	xx
1 INTRODUCTION . . . . .	1
1.1 Sakurajima Volcano . . . . .	3
1.2 The Vulcanian Eruption Process . . . . .	7
1.3 Infrasound Wave Propagation . . . . .	8
1.4 Volcano Infrasound Studies . . . . .	10
2 DETERMINATION OF VENT-SOURCED INFRASOUND AT SAKURA- JIMA VOLCANO . . . . .	12
2.1 Theory of the F Detector . . . . .	13

2.1.1	The Fisher Statistic . . . . .	13
2.1.2	Fisher Statistic Event Detection . . . . .	15
2.1.3	Detection in the Presence of Correlated Noise . . . . .	16
2.1.4	Synthetic Event Detection . . . . .	25
2.2	Application of the F Detector . . . . .	27
2.2.1	Infrasound Data Collection and Pre-processing . . . . .	27
2.2.2	Event Detection at Showa Crater . . . . .	28
2.3	Detection Results . . . . .	30
2.4	Discussion . . . . .	39
2.5	Summary . . . . .	40
3	INFRA SOUND REPOSE INTERVAL DISTRIBUTION MODELING AND STATISTICAL EXPLOSION FORECASTING . . . . .	42
3.1	Methods . . . . .	47
3.1.1	Repose Interval Distribution Modeling . . . . .	47
3.1.2	Likelihood and Confidence . . . . .	49
3.2	Results . . . . .	52
3.2.1	Probabilistic Explosion Forecasting . . . . .	52
3.2.2	Near-real-time Application . . . . .	52
3.3	Discussion . . . . .	60
3.3.1	Sakurajima . . . . .	60
3.3.2	Physical Processes . . . . .	60
3.4	Conclusion . . . . .	62
	REFERENCES . . . . .	64

## LIST OF TABLES

2.1	Types of error . . . . .	15
3.1	Poisson Assumptions . . . . .	44
3.2	Goodness-of-fit Hypothesis Testing . . . . .	50
3.3	Forecasting Probability Cutoff Values & Statistics . . . . .	56

## LIST OF FIGURES

1.1	Infrasound recordings of Vulcanian explosions at Sakurajima recorded on array KUR July 18-25,2013. . . . .	5
1.2	Map showing Sakurajima Peninsula and infrasound array deployment. The 2 arrays used in this study are circled in green; array orientation at KUR is shown in detail. Topographic profiles are drawn from the vent ( <i>left</i> ) to each array ( <i>right</i> ) (modified from Johnson & Miller 2016). . . . .	6
2.1	Beamforming using Fisher statistic values calculated from 5 minutes of infrasound data at arrays HAR and KUR are plotted as rose plots around each array. Colored rings denote the F statistic distribution peaks for the associated azimuth; very low background scores have been removed for clarity. Hot colors signify high F statistic value and a high number of those values observed. . . . .	17

2.2	a)	<p>Computed theoretical background cumulative distribution functions for a range of numerator and denominator degrees of freedom. The numerator degree of freedom is equal to <math>2BT</math>, and denominator degree of freedom equals <math>2(J-1)BT</math>; <math>B</math> is the signal bandwidth [Hz], <math>T</math> is the duration of the sample window [s], and <math>J</math> is the number of receivers used to calculate F. b) F CDF has been shifted as an example of how a correlated noise source can influence the observed background CDF by raising the observed F values. . . . .</p>	18
2.3		<p>Flow of <i>F_ADAPT.m</i> signal detection algorithm. . . . .</p>	23
2.4		<p>The Adaptive Bias Correction Coefficient is used to scale F statistic scores in the presence of clutter such that the observed 99% of the scaled distribution matches the theoretical distribution. The value converges to near 1 after about 3 hours for even extremely high confidence thresholds. The value converges because scaled values less than <math>F_0</math> populate the observed distribution, raising the 99% to a more optimal value. . . . .</p>	24

2.5	(Main) Receiver Operating Characteristic (ROC) curve displaying the rate of true detections to that of false detections; optimal detection rate is 100% true synthetic event detection with 3.376% false detections. (Top, center) Time series of synthetic eruptions with algorithm detections shown in green; background noise and clutter are shown in red. (Bottom, left) PDF of separated F statistic scores. (Bottom, right) CDF showing the theoretical and observed background F statistic scores; 30s interval detections are shown for the last line of data as green stars. . . . .	26
2.6	Infrasound detections for seven days at Sakurajima. Detected events are shown in green, correlated noise pollution not associated with the volcano is shown in yellow, and non-detections are shown in red. F statistics computed at 15s intervals at array HAR. . . . .	29
2.7	Green represents adaptive F detections, red is non-detections. Line gaps are removed data that either clipped out or was not recording due to data download. (left) The PDF of observed F statistics, and (right) theoretical background F statistic CDF in red and empirical background CDF in blue. . . . .	32
2.8	Three explosion events followed by degassing are identifiable from both signal cross-correlation and calculation of the Fisher statistic. Each explosion is preceded by the absence of detectable acoustic signal. Infrasound waveforms are plotted in excess pressure (Pa), running normalized cross-correlation scores range (-1, 1), and the Fisher statistic is plotted on a $\log_e$ scale. . . . .	35

2.9	A close up of the second explosion tail in Figure 2.8 shows very short duration, low amplitude, discrete events; this study regards transient signals such as these as one single open-vent occurrence, as it is unclear in the coherency scores of any loss of signal; the F statistic remains elevated. . . . .	36
2.10	On the left is an idealized F statistic categorization method using hard cutoff values; while on the right, values are placed in temporal context.	37
2.11	A randomly selected hour of infrasound is shown as a time series in panels a) and b). In panel a), the detection algorithm starts at time zero and moves through the hour at 15 seconds intervals. Panel b) shows the same infrasound time series, but the detection algorithm starts 30 minutes in and loops back through the beginning. Panel c) shows the Adaptive Bias Correction Coefficient (ABCC) value. Black arrows illustrate the first loss of coherent volcano-sourced infrasound seen by the detection algorithm. . . . .	38
2.12	Calculated F statistics for both arrays shown as histograms. N is the number of samples used in each histogram. . . . .	40
3.1	Infrasound beam-stack of recordings at array KUR display clustering of large amplitude explosions. Numbers represent time in hours between explosion cluster centers. Black boxes represent explosion forecasts based on loss of detected vent-sourced infrasound denoted by microphone cross-correlation scores. . . . .	46

3.2	Weibull (orange), Gamma (blue), and Exponential (green) probability distributions are fit to the repose interval data (black line). (a) Empirical survival curve from data fitted with exponential and gamma cdfs; shaded areas represent uncertainty out to $\sigma$ (95% confidence) uncertainty is estimated from the variance of $\mu$ and $\sigma$ distributions produced from 1000 Monte Carlo fits to a randomly selected 75% of the data. (b) All repose intervals (black histogram) are compared with only the repose intervals ending in explosion (grey histogram). . . . .	51
3.3	Survival functions for observed repose intervals resulting in explosions ( <i>red</i> ) and emergent degassing events ( <i>blue</i> ). Green stars show the observed percentage of explosions relative to the total number of events that share similar repose interval times; note the logarithmically increasing bin sizes for repose interval time. Explosion likelihood increases significantly after about 45 minutes of infrasonic quiescence. . . . .	53
3.4	The square of the relative error between each distribution median and the current observed repose interval is used as an objective function to predict explosion probability. The green boxed area represents the area where the observed repose interval is predicted to result in explosive activity using 0.2998 as a cutoff. . . . .	57
3.5	Probability density function shows calculated RSMRS values prior to each detected infrasound event. The blue bars are for detected explosions and orange bars are for non-explosive degassing events; the red dashed line marks a cutoff value that separates 97.5% of non-explosions from 74% of explosions. . . . .	58

3.6	Receiver Operating Characteristic (ROC) curve displaying explosion forecasting results from July 18-25 at Sakurajima Volcano using the RSMRS forecasting variable at various cut-offs. . . . .	59
3.7	Explosions are separated based on both recorded pressure amplitude and quiescent time leading up to the event. Explosions are outlined by red boxes. . . . .	61

## LIST OF VARIABLES

$A$	Anderson-Darling test statistic
$B$	Signal bandwidth [Hz]
$D^*$	Kolmogorov-Smirnov test statistic
$F$	Observed Fisher Statistic value
$F_0$	Fisher Statistic cut-off value
$H_0$	Null hypothesis
$J$	Number of array elements
$K$	Number of events
$L$	Observed repose interval time
$N$	Number of samples
$N_1$	Fisher statistic numerator degrees of freedom
$N_2$	Fisher statistic denominator degrees of freedom
$P(K)$	Probability of observing $K$ number of events in time window $\tau$
$P(X; \alpha, \beta)$	Gamma distribution probability
$P(X; k_w, \lambda)$	Weibull distribution probability
$P_n$	Noise power of beam-stack
$P_s$	Signal power of beam-stack
$P_{99}$	99 <sup>th</sup> percentile of a probability distribution
$P_{FP}$	Percent false positive
$P_{TP}$	Percent true positive
$RSMRS$	Quantitative comparison of likelihoods based on 2 sample populations
$S_N$	Signal-to-Noise Ratio (SNR)
$T$	Sample window time length [s]
$X$	Random variable
$\bar{\mu}_N$	Median repose time resulting in non-explosions
$\bar{\mu}_X$	Median repose time resulting in explosions
$\Delta t$	Change in time
$\vec{s}$	Slowness vector
$\vec{x}$	Position vector
$\alpha$	Shape parameter for gamma distribution
$\beta$	Rate parameter for gamma distribution

$\epsilon_1$	Type I error probability
$\epsilon_2$	Type II error probability
$\hat{c}_{99}$	ABCC scaling factor applied to Fisher statistic values
$\lambda$	Scale parameter for probability distribution models
$\phi$	Some measurable quality, such as pressure
$\tau$	Time window
$c$	Scaling factor applied to Fisher statistic values in (Arrowsmith <i>et al.</i> , 2009)
$f$	Frequency [Hz]
$j$	Array element index
$k$	Wavenumber [ $m^{-1}$ ]
$k_w$	Weibull distribution shape parameter
$l_j$	Time shift applied to array element $j$
$n_0$	Sample starting index
$n_N$	Number of observed non-explosions
$n_X$	Number of observed explosions
$t$	Time
$w$	Weighting function for the Anderson-Darling test
$x$	Realized variable
$x_j(n)$	Pressure amplitude [Pa] of the $n^{th}$ time series sample at array element $j$

## LIST OF ABBREVIATIONS

**ABCC** Adaptive Bias Correction Coefficient.

**AD** Anderson-Darling.

**CDF** Cumulative Density Function.

**GMM** Gaussian Mixture Model.

**KS** Kolmogorov-Smirnov.

**PDF** Probability Density Function.

**PMF** Probability Mass Function.

**RMS** Root Mean Squared.

**ROC** Receiver Operating Characteristic.

**RSMRS** Relative Squared Median Residual Sum.

**SNR** Signal-to-Noise Ratio.

**TCED** Temporal Context Event Detection.

# CHAPTER 1: INTRODUCTION

*“Those who do not remember the past are condemned to repeat it.”*

-George Santayana

*“History doesn’t repeat itself, but it does rhyme.”*

-Mark Twain

The aphorisms above offer insight into the nature of historical pattern emergence with the observation that no two sequence of events are exactly the same and highlight the fact that understanding the past may allow for identification of a recurring series of events. This motivates historical documentation of events as qualitative and quantitative data. In a geophysical sense, natural phenomena and other measurable, observable properties of nature serve as data that allow us to understand physical Earth processes. Analysis of these processes may allow us to forecast future events with some confidence.

Volcanic eruptions are powerful natural phenomena that often occur unpredictably in time and magnitude. Even with timely warnings, volcanic eruptions present danger locally as they produce explosions, lava flows, pyroclasts, and noxious gasses, putting nearby communities and individuals at risk. When hazards such as explosive volcanic eruptions are well understood and clearly defined, risk can be mitigated by lowering

susceptibility to that hazard. This thesis addresses the problem of real-time risk assessment during a period of sustained volcanic unrest through quantification of the short term likelihood of future volcanic activity by analyzing recent and current eruptive activity via infrasound recordings.

Chapter 1 is an introduction to Sakurajima Volcano, the Vulcanian style eruption, and infrasound. Chapter 2 focuses on detecting infrasound activity at Sakurajima Volcano using infrasound data recorded near the active vent in Showa Crater. I show how this type of data is integral for volcano monitoring, in both the public safety and scientific domains. In Chapter 3, the detected infrasound periods are used to build an explosion forecasting model applicable in near-real-time. A statistical model of observed wait times between individual events is constructed to describe the observed activity. As activity is continuously monitored, changes in model parameters describe temporal changes in surficial volcanic activity.

Various probability models have been used to describe observed volcano repose, or quiescent, interval times to aid in eruption forecasting and help describe underlying physical processes; often, multiple models provide a reasonable fit to the observed inter-event time data, leading to ambiguity in expected behavior. Models are sensitive to when, where, and how data is collected; for instance, seismic detection is often not sensitive to the lower extremes of volcanogenic earthquakes, and historical eruptive data is limited by observable evidence. This means intermediate length repose intervals (and eruption events) are statistically more likely to be observed, introducing bias into parameter estimation models. Continuous monitoring via infrasound microphone arrays at volcanoes has the potential to reduce these observational flaws by capturing a more complete record of surficial activity and temporal variations in ac-

tivity. Eruption record completeness also depends on observation timescale. Richter was among the first to describe the inverse relation between magnitude and frequency that is observed for numerous natural phenomena, including earthquakes and volcanic eruptions. At open-vent volcanoes degassing takes on various forms; gas can migrate through pores in surrounding rock, bubbles can surface through lava lakes, or the gas can pressurize resulting in explosive degassing. Often volcanoes exhibit multiple styles of degassing in an eruptive sequence (eruption is defined as expulsion of gas, ash or rock; sequence is defined as a set of related events). Sakurajima Volcano displayed tremor-like degassing as well as explosive degassing during the recorded portion (18-25 July) of the eruptive sequence. The significance of infrasound monitoring extends to differentiating these types of events in order to assess the efficiency of simple machine learning algorithms as event type forecasters during the recording period. The infrasound monitoring period used in this study captures 7 days of activity during a period of sustained unrest at Sakurajima. Eruption activities at Sakurajima during the observation period are limited to Showa Crater and, for the purposes of this study, are assumed to be sourced from the same magma generating process, thus I refer to this interval of activity as an eruptive sequence. Shifts between eruptive behavior have been observed at Vulcan Villarrica, Karymski, and many other volcanoes.

## 1.1 Sakurajima Volcano

Sakurajima is an andesitic stratovolcano that rises from the Aira Caldera forming Kagoshima Bay, Japan. The volcano has three craters (Minamidake, Kitedake and Showa), two of which typically transition in activity (Minamidake and Showa). The vent at Showa crater underwent a long dormancy from 1948 to 2006 when activity resumed. Eruptions at Sakurajima Volcano are typically Vulcanian, characterized

by short-lived, high-amplitude, impulsive explosions sometimes followed by vigorous degassing lasting seconds to hours. Phreatic eruptions in 2006-2007 eventually transitioned to magmatic Vulcanian eruptions in February of 2008. Activity levels at Showa crater increased up to 2011 (Iguchi *et al.*, 2013). Activity has been ongoing at Showa crater with intermittence lasting up to months.

Tilt monitoring (Iguchi *et al.*, 2008; Yokoo *et al.*, 2014), precursory inflation observed from infrasound (Yokoo & Ishihara, 2007; Uhira & Takeo, 1994), and repose interval statistics (Varley *et al.*, 2006) have proven useful in event detection (Ishihara, 1985) and forecasting (Garces, 2000) at Sakurajima. Given the historical trends of ground inflation corresponding to increased eruption rates, it is believed that activity at Sakurajima will continue as long as the shallow magma reservoir recharge continues (Iguchi *et al.*, 2013). Recently, activity has resumed at Minamidake crater as well as Showa (Venzke, 2015). In 2013 Showa was producing tens to hundreds of small eruptions per month. This study focuses on a period of activity during 18-25 July 2013 when activity at Sakurajima was limited to Showa crater. Eruptive activity was comprised of both intermittent, and sustained degassing events as well as explosive eruptions with a wide range of amplitudes (Fig 1.1). Data were recorded on infrasound microphone arrays nearby the Sakurajima's active vent (Fig 1.2).

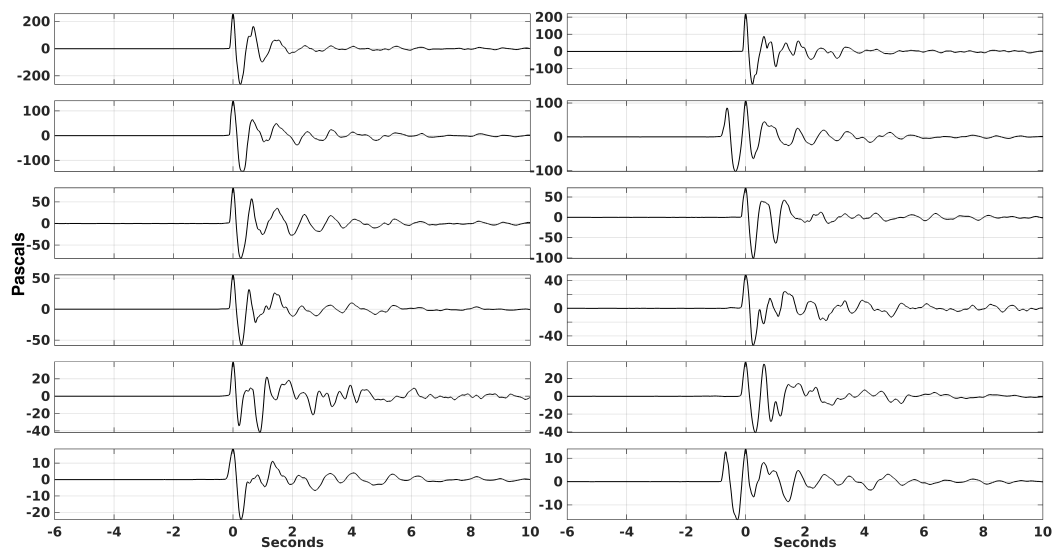


Figure 1.1: Infrasonic recordings of Vulcanian explosions at Sakurajima recorded on array KUR July 18-25, 2013.

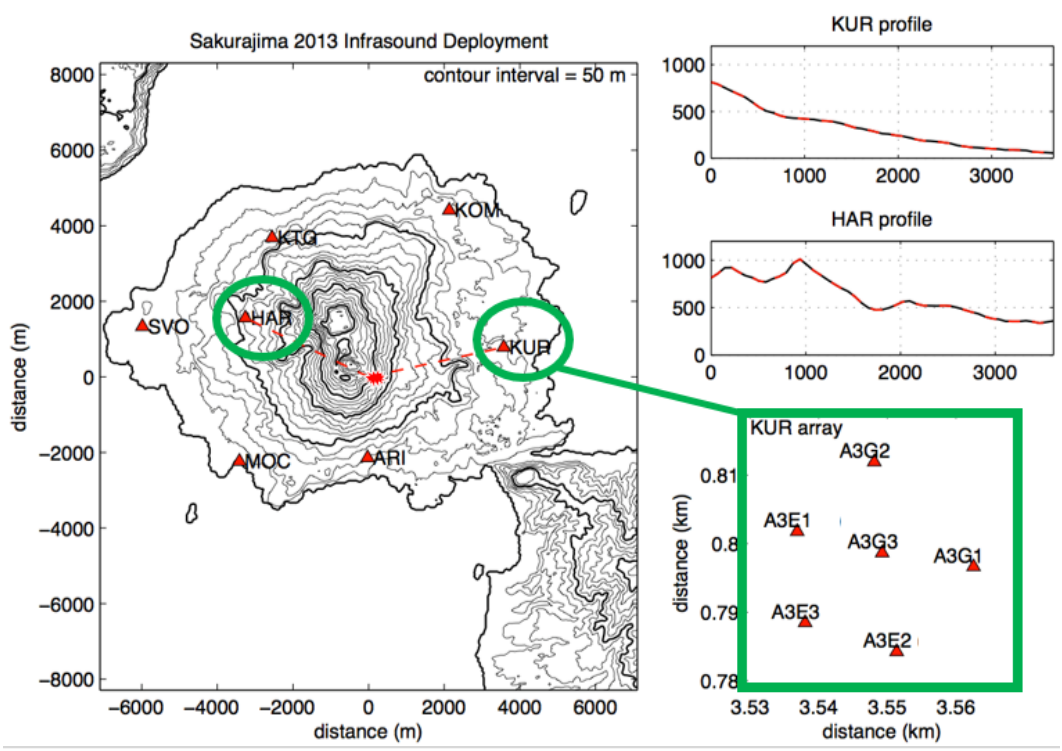


Figure 1.2: Map showing Sakurajima Peninsula and infrasound array deployment. The 2 arrays used in this study are circled in green; array orientation at KUR is shown in detail. Topographic profiles are drawn from the vent (*left*) to each array (*right*) (modified from Johnson & Miller 2016).

## 1.2 The Vulcanian Eruption Process

Gas drives volcanic eruptions. As magma rises, lithostatic pressure (pressure from weight of overlying rock) is reduced and gas bubbles grow in the magma. These bubbles are much more buoyant than the surrounding magma, so they rise. During magma ascent, if there is no room for bubbles to grow, the magma becomes over-pressurized. High viscosity magmas, such as the andesitic magma erupting from Showa Crater, can easily become over-pressurized by hindering bubble growth. This over-pressure often results in violent explosive eruptions, especially near ( $< 10$  km depth) the surface where over-pressures can reach high enough levels to cause spontaneous bubble nucleation. Alternatively, brittle failure of surrounding rock may induce spontaneous bubble formation and growth. This instantaneous depressurization drives gas exsolution/expansion and can cause magma fragmentation. Fragmentation occurs when magma expands so quickly (typically due to rapid decompression) that it reacts as a brittle solid rather than a viscous fluid, and tears apart to form ash and pyroclasts (Alatorre-Ibargüengoitia *et al.*, 2011; Mckee *et al.*, 2014). Subsurface magma movement and eruptions at the surface produce pressure waves that travel through the solid earth (seismic) and the atmosphere (acoustic).

Vulcanian style explosions result from sudden depressurization of a shallow, eruptible, mixture of magma and gas that can result from failure of a viscous/solid cap at the vent surface, stick-slip motion between the magma and conduit walls (Denlinger & Hoblitt, 1999), preferential formation of large waves of gas-rich magma during ascension (Michaut *et al.*, 2013; Cassidy *et al.*, 2015), or interaction with water. At Showa Crater, Uhira & Takeo (1994) observed seismic data from 2 explosive eruptions that lead them to propose a small shallow source of high pressure, presumably gas, as

the explosive source. Local tilt monitoring and sulfur dioxide gas measurements also support the hypothesis of a shallow, gas-rich, magma source. Infrasound monitoring of volcanoes producing Vulcanian style eruptions can provide insight into and allows us to answer questions about the conditions under which these types of explosions occur (i.e. does the vent seal up prior to all explosions?).

### 1.3 Infrasound Wave Propagation

Material or gas erupted during a Vulcanian eruption rapidly displaces air, creating pressure waves that propagate through the atmosphere in all directions as acoustic waves. Low frequency ( $< 20Hz$ ) acoustic microphones are sensitive to atmospheric pressure waves produced during these types of explosions, thus are often used in explosion source and wave propagation studies. Acoustic waves spread spherically as they propagate away from a source. This geometric spreading reduces wave amplitude inversely proportional to distance due to conservation of wavefront energy. At a large (significantly greater than the aperture of a small array of sensors) distance from the source, spherical spreading plays a minor role; the passing of the acoustic wave across each array element can be approximated as a planar wave with no amplitude decay (Rost & Thomas, 2002). It is advantageous to work with slowness ( $|\vec{s}|$ , reciprocal of speed) instead of velocity for many calculations. The plane wave model of a propagating disturbance recorded at a single location is given below (1.1).

$$\phi(\vec{x}, t) = e^{(2\pi i f(\vec{s} \cdot \vec{x} - t))} \tag{1.1}$$

$\phi(\vec{x}, t)$  represents a measurable quantity that is disturbed by a planar wavefront perpendicular to  $\vec{s}$ , at location  $\vec{x}$ , with frequency  $f$ . The slowness vector,  $\vec{s}$ , describes

the direction and slowness (in  $s/m$ ) of the wave. The plane wave approximation simplifies calculations for expected arrival time differences from the source (Showa Crater) to each receiver (1.2). Acoustic waves undergo frequency dependent dispersion, where high frequencies travel slower than low frequency components. This effect is commonly ignored for low frequency waves in the atmosphere because the effect is very slight.

With these simplifying assumptions, the only difference between volcano-acoustic waves at each receiver is a time shift. To detect coherent energy, traces from each microphone are shifted and stacked according to the expected plane wave arrival time calculated from source-receiver geometry (1.2). Travel time ( $t$ ) of an acoustic wave from source to receiver can be calculated using equation 1.2, where  $\vec{s}$  is slowness in  $s/m$  and  $\vec{x}$  is the position vector of the recording device relative to the source location.

$$t = \vec{s} \cdot \vec{x} \tag{1.2}$$

Expected travel time differences are calculated using a known source location, array orientation, and slowness vector by subtracting travel times from one receiver from another (1.3).

$$\Delta t = \vec{s} \cdot \vec{x}_1 - \vec{s} \cdot \vec{x}_2 \tag{1.3}$$

Alternatively, travel time differences between array elements can then be used to

calculate the slowness of incoming waves (Eq 1.4).

$$\vec{s} = \frac{\Delta t}{\vec{x}_1 - \vec{x}_2} \quad (1.4)$$

## 1.4 Volcano Infrasound Studies

Seismicity has been widely used for volcano monitoring (Kanamori *et al.*, 1984; Kawakatsu *et al.*, 1992; Morrissey *et al.*, 2008; Sanderson *et al.*, 2010; Ichihara *et al.*, 2013; Miwa & Toramaru, 2013; Matoza *et al.*, 2014; Ripepe *et al.*, 2015; Lyons *et al.*, 2016). However, it is often the case that acoustic waves recorded on nearby microphone arrays are more representative of the surface out-gassing process because waves propagating through the atmosphere are less altered than waves traveling through the subsurface (Garces, 2000). Acoustic waves propagate through a significantly more homogeneous atmosphere and experience minimal scattering compared to the highly heterogeneous layered subsurface that seismic waves travel through.

Volcanoes produce the majority of their acoustic energy in the infrasound (below 20Hz) frequency band (Johnson *et al.*, 2004; Garces, 2000; Ripepe *et al.*, 2007). Infrasound microphones record a high-pass filtered version of atmospheric perturbations produced by local or regional acoustic events, such as surficial volcanic activity, rock fall, thunder, and ocean wave oscillations (Marcillo *et al.*, 2012; Anderson *et al.*, 2018). Infrasound array processing techniques have been established for small-aperture microphone arrays, as well as regional microphone networks, similar to seismic array processing. Acoustic wave properties such as speed and propagation direction can be calculated from coincident microphone recordings using techniques such as cross-correlation (Johnson, 2004; Matoza *et al.*, 2018). This infrasound data has been used

in previous research towards acoustic source localization and characterization (Kim & Lees, 2014; Mckee *et al.*, 2014; Yokoo *et al.*, 2014), quantifying explosive volume of erupted material (Johnson & Miller, 2014), and acoustic explosion characterization (Matoza *et al.*, 2014). Fee *et al.* (2014) composed a detailed introductory paper focused on the open source dataset discussing how the data was collected, how the infrasound microphones behave, and displaying event detections for highly correlated ( $> 0.5$  correlation coefficient) infrasound over 10 s windows.

Infrasound has been used to detect and catalog volcanic eruptions at many volcanoes (Matoza *et al.*, 2014). Volcanic explosions are detectable from infrasound recordings at local ( $< 10\text{km}$ ) and sometimes regional ( $< 500\text{km}$ ) distances. Important statistics can be calculated from volcano infrasound, including event amplitude and duration (Varley *et al.*, 2006), acoustic signal frequency, and the rate at which events occur over time. For the problem of event forecasting, the most useful statistic is the arrival rate. The arrival rate is defined as the most probable number of events that can be expected in a given amount of observation time. Inversely, we can use the arrival rate to estimate the expected wait time between events. Data are typically viewed as a histogram, or Probability Mass Function (PMF). The PMF shows the relative probabilities of quiescent time lengths prior to events based on past records. If an eruption sequence is monitored for long enough, the distribution of number of events versus time will illuminate a probability model of what can be expected based on previous observations. A more standard description of probability is the Probability Density Function (PDF), which takes the width of each bin into account to estimate probability by dividing by the width of each bin.

## **CHAPTER 2:**

# **DETERMINATION OF VENT-SOURCED INFRASOUND AT SAKURAJIMA VOLCANO**

To robustly detect eruptive activity I use an objective, systematic, signal processing algorithm capable of real-time application. Infrasound recordings from arrays HAR and KUR are used to detect eruptive activity from Showa crater at Sakurajima volcano by quantitatively measuring the similarity between microphone recordings in a way that both highlights vent-sourced signals and identifies other possible sources of correlated signals not sourced from the vent of interest (Showa Crater). Correlated noise such as this is referred to as clutter.

Expected time shifts for acoustic waves sourced from Showa Crater are calculated for each microphone according to Eq. 1.3 such that when the time shifts are applied to the recordings, infrasound produced from the volcano arrives at the same instant on all microphones. Under plane wave assumptions each microphone records the same acoustic wave such that stacked recordings will sum constructively. Acoustic waves that propagate across the microphones at different speeds or directions will stack destructively. In order to quantitatively discriminate further against off-axis infrasound waves, I calculate a ratio of constructive signal power to random noise power using the Fisher statistic.

## 2.1 Theory of the F Detector

### 2.1.1 The Fisher Statistic

The similarity of infrasound recordings is quantified using a test statistic called the Fisher Statistic ( $F$ , Eq. 2.1).

$$F = \frac{(J - 1) \sum_{n=n_0}^{n_0+(N-1)} [\sum_{j=1}^J x_j(n + l_j)]^2}{(J) \sum_{n=n_0}^{n_0+(N-1)} [\sum_{j=1}^J x_j(n + l_j) - [\frac{1}{J} \sum_{m=1}^J x_m(n + l_m)]]^2} \quad (2.1)$$

Derived from the analysis of variance, the Fisher Statistic measures the similarity of multi-channel time series data as a ratio of stacked power over residual power. In equation 2.1,  $J$  is the number of receivers used in the beam-stack,  $N$  is the number of samples in each calculation interval,  $x_j(n)$  is recorded amplitude of sensor  $j$ , and  $n_0$  is the starting index for each interval.  $l_j$  is a time shift applied to each trace to achieve maximum stacking amplitude for signals of a desired slowness. If the source location is unknown, slowness can be varied and the corresponding F statistic can be used to determine the probability of a coherent signal propagating from a particular direction. Once the recordings at each microphone are shifted according to a certain slowness, signals coming from the correct azimuth and at the correct wave speed will be more likely to produce a high F statistic. Signals from other sources will cross the array with different speeds and azimuths; thus, calculated F statistic values will be severely penalized due to the squared sum of the deviation about the mean signal in the denominator.

A process can be parameterized by how often events occur. An informative way to display this type of frequency data is in a histogram, or similarly a Probability Density Function (PDF); a PDF is similar to a PMF, except a PDF takes each bin

width into account when calculating the probability of observing a value in that bin. An important aspect of the Fisher Statistic is the theoretical PDF described by Fisher *et al.* (1943). Fisher's logarithmic series distribution, the F distribution, describes the probability of observing any F statistic score in the presence of random Gaussian noise. The theoretical (background/expected) PDF can be constructed from the known degrees of freedom ( $N_1 = 2BT$  for the numerator and  $N_2 = (J - 1)N_1$  for the denominator) and noncentrality parameter  $\lambda = 2BT(S_N)^2$  (Shumway, 1971).  $S_N$  is a (typically) unknown Signal-to-Noise Ratio (SNR),  $J$  is the number of channels,  $B$  is the signal bandwidth, and  $T$  is the window length used for calculation. The noncentrality parameter is used to shift the F distribution along the abscissa in order to maintain the associated Type I error probability during periods of non-Gaussian distributed background noise. In theory, this allows me to implement a cutoff value of the test statistic F such that scores above the cutoff are considered volcanogenic signals, while lower scores are indicative of noise not associated with the volcanic vent (background noise).

The survival function (Eqn. 2.2) of expected Fisher statistics determines the likelihood that the value represents signal other than random Gaussian noise as proposed by the theoretical distribution. This curve provides statistical confidence (i.e., 75%, 90%, 95%, 99%, *etc.*) that any observed F score indicates a source other than random chance. Fisher *et al.* (1943) shows how the F distribution is related to the Poisson distribution under certain simplifications. Both distribution models belong to the exponential family.

$$\textit{Survival Function} = 1 - \textit{CDF} \tag{2.2}$$

**Table 2.1: Types of error**

		$H_0$ True	
		False	True
$H_0$ Inference	False	True Positive	False Positive ( $\epsilon_1$ )
	True	False Negative ( $\epsilon_2$ )	True Negative

### 2.1.2 Fisher Statistic Event Detection

Melton & Bailey (1957) first suggested the F statistic as a signal detector in 1957 where he used it to detect simulated seismic wave forms. Booker & Backus (1965) first showed the mathematics in matrix form and proposed a robust automatic seismic detection method using a statistically relevant threshold value of the F statistic to differentiate scores indicative of signal from those that arise from random chance in the presence of no source. He also described two parameters that describe Type I (Eq. 2.3) and Type II (Eq. 2.4) errors, false positive detection and false negative event detection, respectively which are used to measure the goodness of the signal detector. Types of error are shown in Table 2.1, commonly referred to as the confusion matrix.  $\epsilon_1$  and  $\epsilon_2$  are described in terms of signal detection using a threshold ( $F_0$ ) for statistical significance.

$$\epsilon_1 = Prob\{F > F_0 \mid F \in I\} \quad (2.3)$$

$$\epsilon_2 = Prob\{F < F_0 \mid F \in II\} \quad (2.4)$$

$F_0$  is a cutoff value typically chosen to represent the 95<sup>th</sup> or 99<sup>th</sup> confidence level based on the calculated background F distribution.

The F statistic can be used in frequency-wavenumber (f-k) analysis, commonly re-

ferred to as ‘beam forming’, which calculates the direction and speed of wave energy that produces the highest F statistic value. Beam-forming is useful for differentiating between various sources if they differ in location, frequency, or wave speed; an interested reader can find a detailed background on f-k analysis from Rost & Thomas (2002). Beam forming calculates an F statistic value for various time shifts  $l_j$  to simulate many slowness vectors that have an azimuth and wave speed associated with them; for a visual representation refer to figure 2.1.

### **2.1.3 Detection in the Presence of Correlated Noise**

The F detector is robust under the assumption of a constant noise level (Shumway, 1971) (Abramowitz & Stegun, 1972). A Gaussian background noise distribution is typically assumed for identifying signal using the F statistic. When background noise is correlated across array elements the statistical likelihood that a high F statistic (above  $F_0$ ) will be observed in the absence of signal of interest (vent-sourced infrasound) increases. Sources of correlated noise, also called clutter, include ocean waves, industrial anthropogenic noise, vehicle noise, man-made explosions, etc. Correlated noise shifts the background F distribution towards higher scores, inconsistent with the theoretical background CDF (Fig. 2.2). Clutter may also impact the shape of the F distribution, complicating the link to Fisher’s theoretical distribution of signal coherence.

Douze & Laster (1979) modeled signal to correlated noise ratios and laid out assumptions necessary to approximate the background F-statistic in the presence of correlated noise. The results show expected false alarm rate for various signal to correlated-noise ratios of the beam (time-shifted, stacked signal).

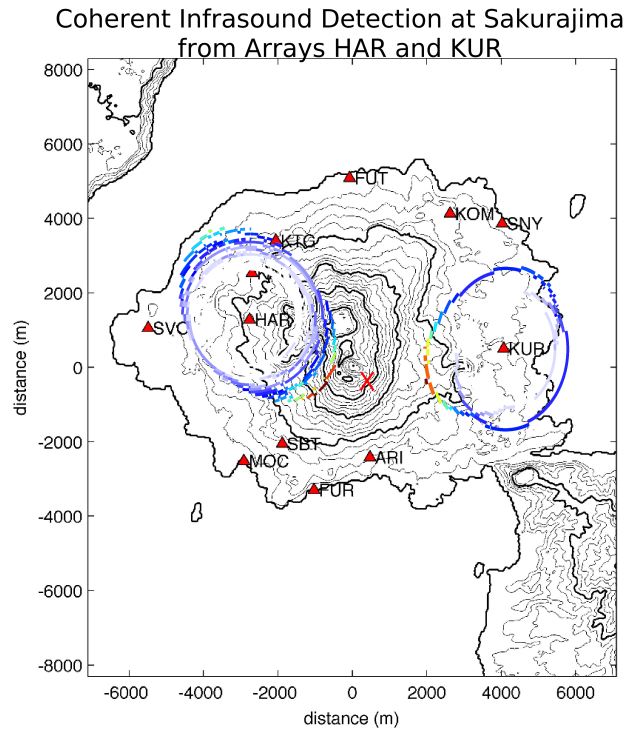


Figure 2.1: Beamforming using Fisher statistic values calculated from 5 minutes of infrasound data at arrays HAR and KUR are plotted as rose plots around each array. Colored rings denote the F statistic distribution peaks for the associated azimuth; very low background scores have been removed for clarity. Hot colors signify high F statistic value and a high number of those values observed.

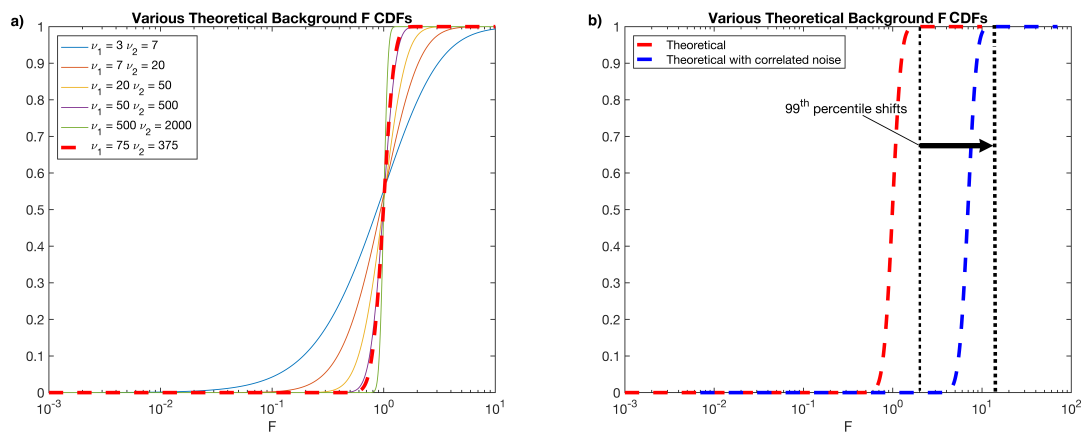


Figure 2.2: a) Computed theoretical background cumulative distribution functions for a range of numerator and denominator degrees of freedom. The numerator degree of freedom is equal to  $2BT$ , and denominator degree of freedom equals  $2(J - 1)BT$ ;  $B$  is the signal bandwidth [Hz],  $T$  is the duration of the sample window [s], and  $J$  is the number of receivers used to calculate  $F$ . b)  $F$  CDF has been shifted as an example of how a correlated noise source can influence the observed background CDF by raising the observed  $F$  values.

Booker & Backus (1965) and Arrowsmith *et al.* (2009) displayed two methods for adapting the detector to correlated noise in the signal band. Booker (1965) hypothesized that simply raising the detection threshold will produce less false positives during periods of correlated noise. This is intuitive, but raising the threshold ( $F_0$ ) increases the likelihood of Type II errors for faint coherent signals. Arrowsmith *et al.* (2009) used a moving adaptive window that encapsulates the entirety of the correlated noise period and applies a scaling factor  $c$  (Eq. 2.5) to all coherency scores in the observation window such that the peak associated with unwanted correlated noise sources matches the peak of the theoretical background PDF with no correlated noise source. A smaller moving window that runs inside the larger adaptive window is used to detect F scores outside of the background PDF and count them as signal (Arrowsmith *et al.*, 2009).

$$c = \left(1 + J \frac{P_s}{P_n}\right) \quad (2.5)$$

F statistics in the large adaptive window are scaled by  $c$ , where  $J$  is the number of array elements,  $P_s$  is the signal power of the beam stack, and  $P_n$  is the noise power of the beam stack. The Signal-to-Noise Ratio (SNR)  $P_s/P_n$  is often unknown in nature, which is why other graphical and statistical methods have been explored (Blandford, 1974). Scaling the F statistic values to match the theoretical background pdf allows for the statistical threshold value to remain unchanged throughout the observation period; this is important for assessing the confidence of detections. A problem with this method is that the F statistic probability distribution is assumed to have the same shape as the observed F PDF with correlated noise sources, as displayed on the right in figure 2.2. In my observed distribution of infrasound F scores at Sakurajima this assumption is invalid; correlated noise F statistic distribution has a wider log-

normal distribution which would give rise to a high false positive rate using the peak matching method.

The adaptive window used by Arrowsmith *et al.* (2009) also increases the likelihood of Type II errors by scaling possible true signal F scores below the detection threshold  $F_0$ . Additionally, this approach has the potential for Type I errors (false positives) in the case where correlated noise events are shorter than the adaptive window length. In this scenario a short instance of correlated noise may be regarded as true signal. Rigorous tuning would likely be required for each dataset for detection of specific events.

The adaptive F detector that I employ operates on a null hypothesis that the observed statistic comes from the empirically constructed background PDF, or scaled ‘clutter’ PDF. I apply a method similar to Arrowsmith *et al.* (2009) where calculated F statistics are scaled to fit the theoretical background PDF. However, instead of matching the peak of the theoretical background distribution to the observed clutter F statistic probability distribution peak, I match the 99% confidence bound of the expected F statistic background CDF to that of the observed CDF; this produces a statistically robust threshold value for F that is largely independent of the observed distribution shape.

The observed F statistic distribution shape can not be matched by a translation of the expected background F scores. If this were the case then matching the peak of the observed distribution to the theoretical one would be optimal because all statistical relevance would be maintained by the scaling of Fisher statistics. In the case where the distribution shapes are not similar, peak matching will not ensure that the percentiles of the observed distribution are statistically accurate when compared to

the theoretical F distribution. This can be seen in Figure 2.4 where the distributions associated with clutter are distributed log-normally. To maintain the the highest level of statistical accuracy, the observed distribution should be scaled to match the percentile of interest (statistical detection threshold). This will ensure the correct confidence based upon Fisher’s theoretical distribution.

The theoretical CDF is used as *a priori* information to assess an initial F statistic cutoff. As data is passed through the detection algorithm, the observed background CDF is updated. A bias correction, necessary in the presence of correlated noise, is applied to match the 99% confidence bound of the theoretical CDF. This automated process uses only a selected confidence bound and the theoretically calculated F CDF to self-regulate detections. Results can be computed for any necessary confidence level. The Adaptive Bias Correction Coefficient (ABCC),  $\hat{c}_{99}$ , is continually updated as data is passed through the algorithm and takes the form

$$\hat{c}_{99} = \frac{P_{99}(CDF_{Theory})}{P_{99}(CDF_{Obs})} \quad (2.6)$$

This value is used to scale calculated F values such that F scores produced from clutter are not counted as vent-sourced signal. As stated before, clutter will raise all observed F statistic scores. The ABCC is updated as scores below the current F cutoff value populate the observed background PDF, raising the 99% F value which is analogous to raising the ABCC. Statistical significance is preserved at a known confidence level. This is important because it does not require a known signal-to-noise ratio or an expected level of clutter. It is only necessary that the experimental setup (source-receiver geometry, setting, signal bandwidth, etc.) ensures that the

signal of interest has the highest statistical likelihood for producing the highest F statistic. There should also be a gap between the distribution of F scores produced from clutter and those produced from the source to be monitored. This should be achieved if the experimental setup is optimized for signals of interest, however may not be achievable in circumstances of low signal power compared to background noise. One extremely valuable feature of this routine is the discrimination between different sources located in the same direction relative to an array. Since signal power is an element of the F statistic, sources with different amplitudes will have their own F statistic distribution, that may overlap, but should be distinct from each other. This will be shown later on when I discuss F statistic distributions observed at array KUR.

The *F\_ADAPT.m* algorithm (Fig 2.3) does not use the detected F score values so as to never limit the percentage of detections to total number of data; only sufficiently low scores are used for constructing the empirical background PDF. The ABCC is shown to quickly converge to an ideal scaling factor very close to one after a few minutes of processing recordings that contain elevated background scores. A value greater than one is expected to maintain statistical confidence in the observed background PDF. This value may continue to change depending on how populated the observed background PDF becomes, the ABCC will vary accordingly. The scaling factor is only applied to the next set of calculated F statistics. The value quickly approaches, but does not reach, one because the F scores that populate the observed F distribution are descaled (multiplied again by the ABCC). This allows for quick convergence (Fig 2.4) and eventual redundancy of the ABCC, as the 99% is very sensitive to high F scores in the distribution and remains fairly insensitive to low and moderate values. Early on, when the ABCC is  $\gg 1$ , the values that populate the

background F distribution raise the 99% to its optimal value.

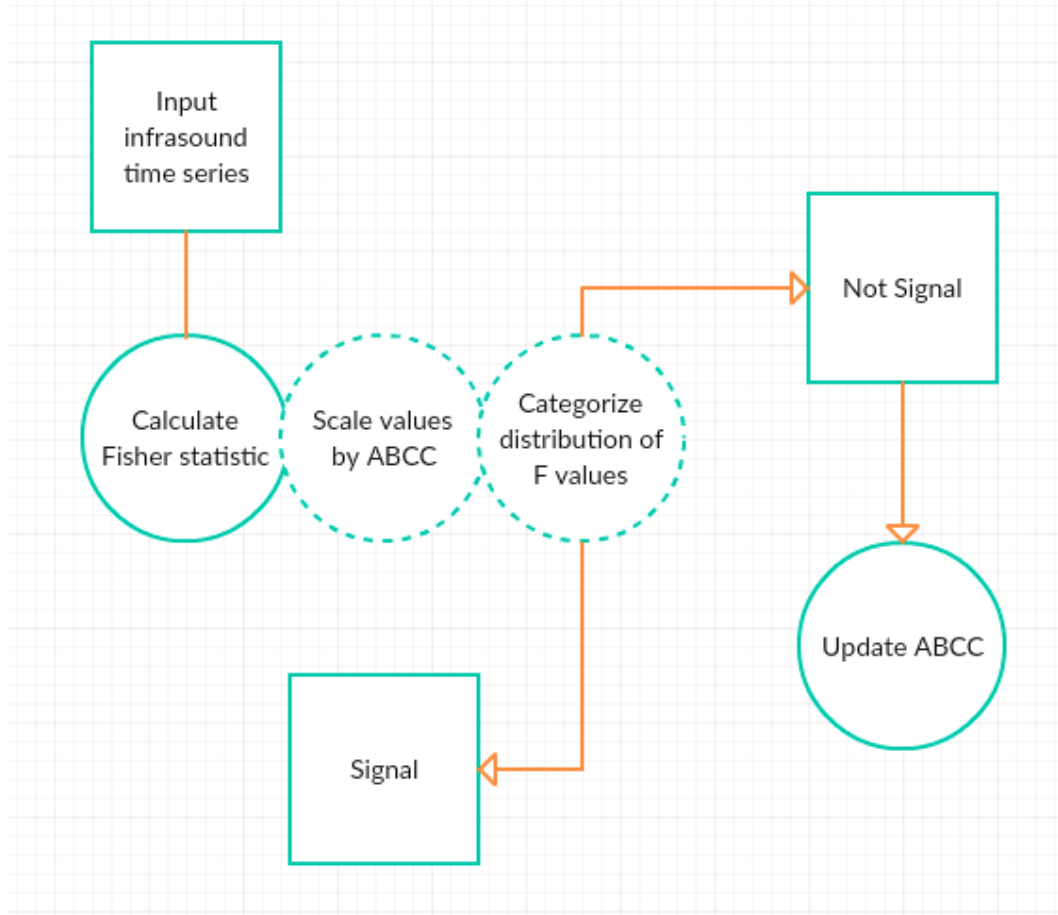


**Figure 2.3: Flow of  $F\_ADAPT.m$  signal detection algorithm.**

The ABCC can be considered the non-centrality parameter, as it described the relationship between the theoretical and observed background PDFs as a linear shift about the abscissa. The ABCC converges to a value necessary to uphold the statistical confidence of signal detection, given clutter in the signal. If there is no clutter, the value of  $\hat{c}_{99}$  should be one.

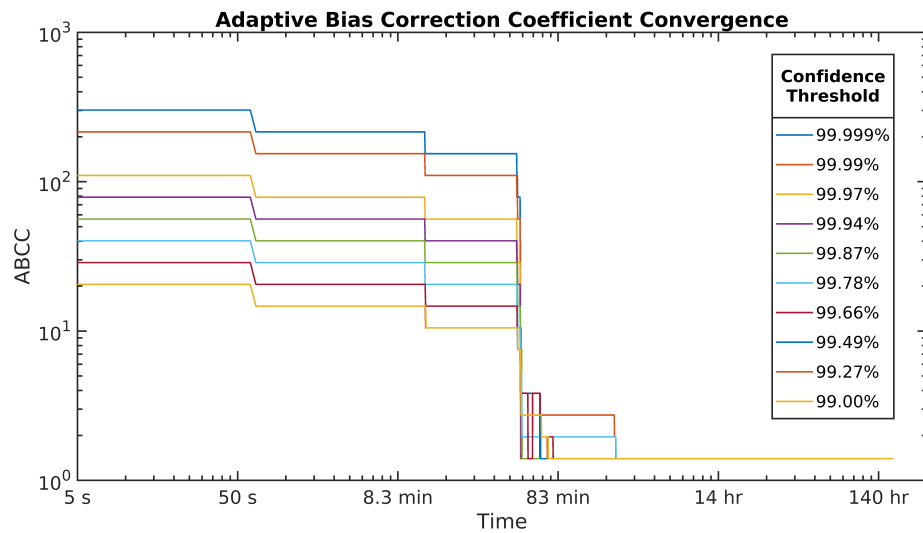


Figure 2.4: The Adaptive Bias Correction Coefficient is used to scale  $F$  statistic scores in the presence of clutter such that the observed 99% of the scaled distribution matches the theoretical distribution. The value converges to near 1 after about 3 hours for even extremely high confidence thresholds. The value converges because scaled values less than  $F_0$  populate the observed distribution, raising the 99% to a more optimal value.

### 2.1.4 Synthetic Event Detection

The adaptive algorithm was tested on synthetic data. I constructed synthetic recordings by convolving a characteristic Sakurajima eruption waveform with a time series of spikes at semi-regular intervals; Gaussian noise was added to each synthetic recording at a SNR of about 4, and  $2.5Hz$  sine waves were added to the second half of each trace to represent correlated noise. The synthetic time series and associated F scores are shown in Figure (2.5), along with a Receiver Operating Characteristic (ROC) curve that was constructed using the synthetic data. This curve shows the true detection rate to the false detection rate for various statistical cutoff values; the value I used was 0.99. The resulting 3.376% false positive detection rate aligns with results from a study by Wirth *et al.* (1971), which modeled expected detection statistics using the Fisher statistic for various beam stack Signal-to-Noise Ratios as a function of the number of array elements and signal and ambient noise characteristics.

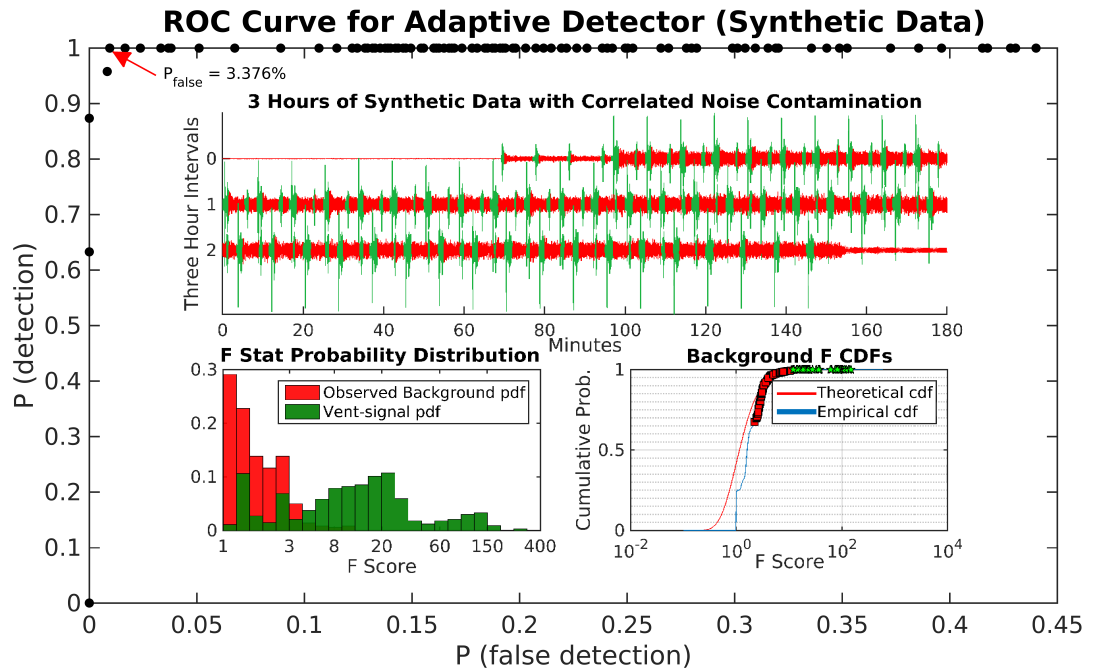


Figure 2.5: (*Main*) Receiver Operating Characteristic (ROC) curve displaying the rate of true detections to that of false detections; optimal detection rate is 100% true synthetic event detection with 3.376% false detections. (*Top, center*) Time series of synthetic eruptions with algorithm detections shown in green; background noise and clutter are shown in red. (*Bottom, left*) PDF of separated F statistic scores. (*Bottom, right*) CDF showing the theoretical and observed background F statistic scores; 30s interval detections are shown for the last line of data as green stars.

## 2.2 Application of the F Detector

### 2.2.1 Infrasound Data Collection and Pre-processing

Two infrasound microphone arrays (KUR and HAR) recorded quasi-continuously on the eastern and western flanks of Sakurajima Volcano from July 18 - 25, 2013. Both arrays were approximately 3.5km away from the active vent (Showa Crater). Array KUR comprised six microphones on the eastern flank with line of sight of the crater edifice. Array HAR comprised three microphones on the western flank behind substantial topography. Both arrays were approximately 30m in diameter, all instruments used in this study were InfraBSU infrasound microphones with a corner frequency (3dB down) of  $0.04Hz$  connected to 24-bit Omnirecs DATA-CUBEs recording at 200 Hz (Fee *et al.*, 2014). Microphone details are similar to those discussed in Marcillo *et al.* (2012).

The recorded infrasound data contains signals from volcanic activity at Sakurajima, but also records pressure variations from ocean waves crashing on the shore, wind, thunder, ambient temperature and pressure changes, anthropogenic (industrial and vehicular) activity, and much more. One of the goals of the infrasound array deployment was to test topographic effects on infrasound wave propagation, using eruptive activity at Sakurajima as a source. In this study, I use the two infrasound arrays to identify volcanic infrasound signal among other sources of infrasound to determine when the vent at Showa Crater is actively producing infrasound.

In order to study the volcanogenic infrasound data, I filter the recordings between 0.5 and  $3Hz$  using a 2-pole Butterworth filter. This helps remove signals unrelated to the volcano that contaminate the data such that the data is representative of

volcanic activity. However, there is still noticeable wind (and other) noise present in the infrasound data within the frequency band of the volcano infrasound.

### **2.2.2 Event Detection at Showa Crater**

In the theory of the F statistic, it is assumed that there exists a cutoff separating background noise (and clutter) from the signal of interest such that F statistics indicative of signal are statistically identifiable. The separation of F statistics by multiple sources is evident in the total observed F PDF (Fig 2.6) for the 7 days of data, I regard these sources as random background noise, off-axis correlated noise (clutter), and vent-sourced signal. A single F statistic is calculated at each sample point of the infrasound recordings. Each calculation, however, represents the F statistic from 15s of data ( $15s \times 200 \frac{\text{samples}}{s} = 3000$  samples). The observed F statistic PDF is trimodal, suggesting three signal contributions. I use beam-forming at array HAR to differentiate acoustic energy associated with nearby Kagoshima city from the acoustic signal from Showa Crater. These sources are in opposing directions at array HAR, however at array KUR the active volcanic crater is in the same direction as the city. Energy from these sources is indistinguishable from beam-forming calculations at array KUR. Beam-forming results show that the central peak of the F distribution is most likely associated with correlated noise from the direction of Kagoshima city.

To obtain the categorized F statistic results I use Temporal Context Event Detection (TCED). TCED places F statistic scores in temporal context, like a time-average. Temporal analysis is necessary due to the impulsive nature of wind gusts and other infrasound noise that produce intermittent detections during periods of probable, sustained, low amplitude infrasound signals at Showa Crater. This low amplitude volcanic infrasound interrupted by higher amplitude incoherent noise (wind) differs

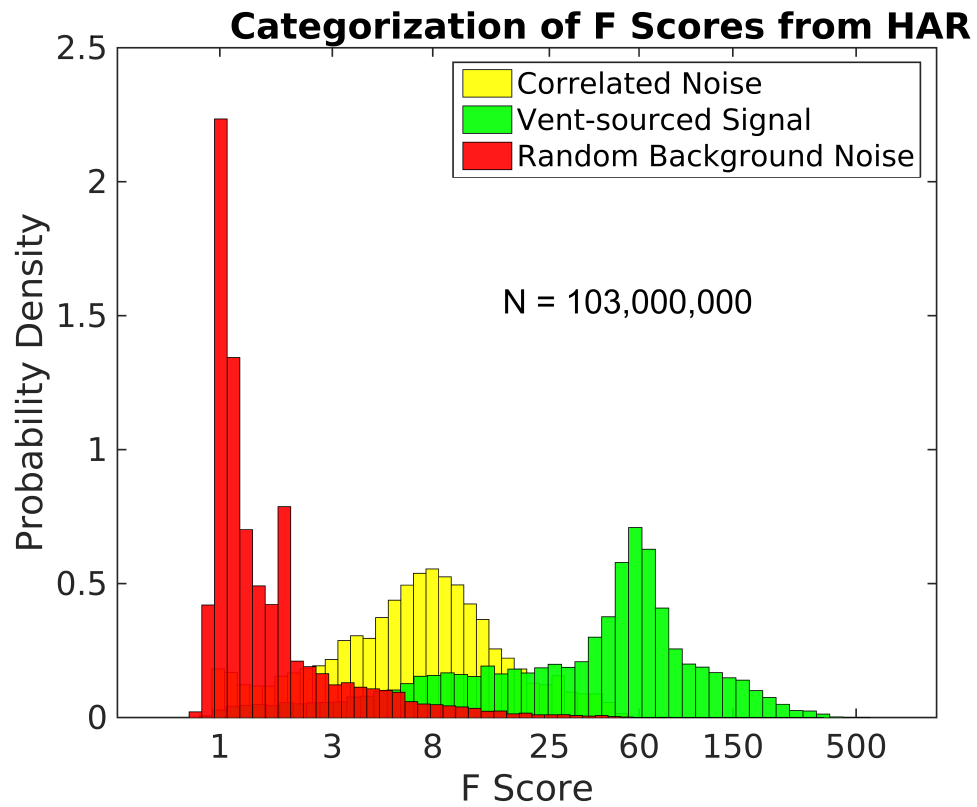


Figure 2.6: Infrasound detections for seven days at Sakurajima. Detected events are shown in green, correlated noise pollution not associated with the volcano is shown in yellow, and non-detections are shown in red. F statistics computed at 15s intervals at array HAR.

distinctly from periods of intermittent signal separated by extremely low amplitude (negligible) ambient noise. Diurnal patterns of variable wind noise are noticeable in the infrasound data. To combat this artifact, I look at the distribution of F statistics over a short time window (30s) to get a better representation of the context of each F score. Thus, a loss of loss of vent-sourced signal lasting less than 30s is disregarded, yielding more plausible detection results during windy periods. Although wind noise can produce short bursts of incoherent infrasound, F statistic scores for low amplitude degassing events are still well above those produced from clutter. The inclusion of intermittent low F values is displayed in figure 2.6 as the left tail of the vent signal PDF extends into the background noise PDF. This rectification lowers the amount of signal detection intervals from 726 down to 366.

## 2.3 Detection Results

Detections at each array are used in conjunction to determine coherent infrasound originating from the vent accounts for 54.4% of the acquisition duration at 99% confidence, using the adaptive bias correction coefficient scaling method. Explosive eruptions and degassing immediately following explosions take up one third ( $\frac{1}{3}$ ) of the total open-vent duration. Repose intervals (quiet periods where no infrasound is detected) range from 1 to 400 minutes in duration. Prior to all 28 detected explosions (defined here as an impulsive compression greater than 3.5 Pa recorded peak amplitude followed by a subsequent rarefaction) the absence of vent-sourced infrasound is observed on both arrays. Figure 2.7 shows the resulting 726 detections from the adaptive F detector in green, and non-detections in red, for the week long observation period. From the 3.376% false detection rate found from the ROC curve constructed from synthetic data, I estimate a false alarm rate of approximately 2

events/day for the 366 detections over 7 days (an estimated 14 total misdetections). This estimate assumes that the Signal-to-Noise Ratio (SNR) remains around 4 to 1 for volcanic signal, according to work done by (Wirth *et al.*, 1971).

One goal of this study was to determine when the volcanic vent is closed. Unfortunately, the presence of clutter hinders the ability to confidently determine all periods of vent closure solely from infrasound data. Another problem with measuring the F statistic to determine signal coherence is multipath affects, such as waveform reflections that may propagate across the acoustic array at various apparent wave speeds and direction. These reflections are a likely cause for intermittent reduction of coherency scores during, or shortly after, an infrasonic event. An observation supporting this idea of interference is observed on array KUR when, just after an identified explosion at Showa Crater, coherent signal is detected from an azimuth associated with mountainous topography a few miles southeast of KUR. From this observation I assume error in some of the short repose intervals, especially when distinct periods of moderately high amplitude, tremor-like degassing are interrupted for brief ( $< 1$  min) periods while Root Mean Squared (RMS) amplitude is sustained (Fig 2.8). Theoretically this affect would be minimized by the presence of two independent arrays, but unfortunately array HAR is much less comprehensive in detections.

Figure 2.8 displays three explosions, each preceded by no detectable acoustic signal. I attribute the lack of coherent vent-sourced infrasound to a sealing of the vent by a viscous cap at the surface, such as the model proposed by Woods (1995). High frequency (0.5 – 1 Hz) transitions from open to close (and vice-versa) are observed during supposed sustained volcanic degassing (Fig 2.9) that requires a fluid cutoff value for event detection, less there be multiple detections per single out-gassing

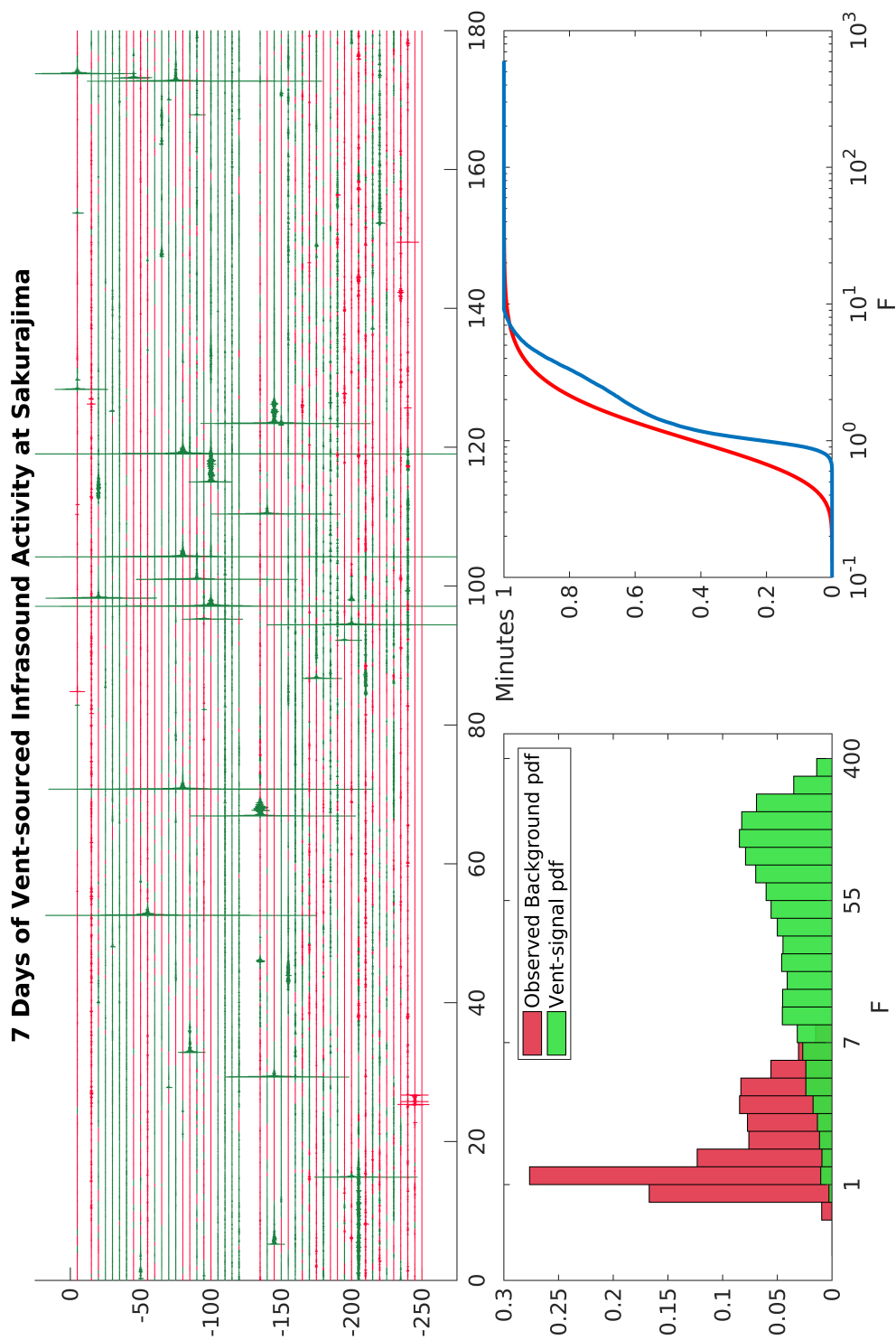


Figure 2.7: Green represents adaptive F detections, red is non-detections. Line gaps are removed data that either clipped out or was not recording due to data download. (left) The PDF of observed F statistics, and (right) theoretical background F statistic CDF in red and empirical background CDF in blue.

event. Rather than observing  $F$  statistics as independent values, uncorrelated with neighboring values, I observe the distribution of other  $F$  values local to the each value in question such that the value is put in a temporal context. This requires me to choose a representative time duration to determine vent status (opened or closed) of 1 minute. From this time-based signal detection scheme I obtain  $F$  statistic categorization results that reflect reality, opposed to an idealistic Gaussian Mixture Model (GMM) result (Fig 2.10).

The correlated noise identified in the  $F$  statistic PDFs for each array is assumed to be anthropogenic noise from Kagoshima, where a city and busy port are located just  $8km$  from the volcano. Array HAR, located on the eastern flank of Sakurajima, between the city and volcano, allows for robust distinction between city- and vent-sourced signals. At array KUR the Showa crater vent shares a common azimuth with Kagoshima, introducing difficulties in differentiating clutter from vent-sourced signal at array KUR using techniques like beam-forming or cross-correlation. However, the magnitude of the  $F$  statistic can be used to differentiate between these two sources, even in the instance of a shared azimuth relative to the microphone array.

Since I am focused on real-time, automated, volcano-acoustic event detection to be used for forecasting, the value that the ABCC converges on is not enacted on previously processed data. This means that early detections have a higher chance of containing false positive detections until the ABCC converges to a statistically robust value. In other words, if the detection algorithm started in the middle of the 7 day dataset and then looped back to the first half, detection results may differ slightly, however, figure 2.11 illustrates how minimal this affect is on detection precision. In panel a) the adaptive detection algorithm is used on one hour of recorded infrasound;

in panel b) the one hour infrasound time series is run through the algorithm starting 30 minutes in, and then ending with the first 30 minutes. Signal determined to be sourced from Showa Crater is plotted in green for each time series, while clutter and background noise are shown in red. ABCC convergence for each case is shown in panel c). Convergence is quicker for the first case only because the second case contains constant volcanic signal for about 18 minutes. The detection of coherent signal well above the expected background pdf does not affect the bias correction coefficient.

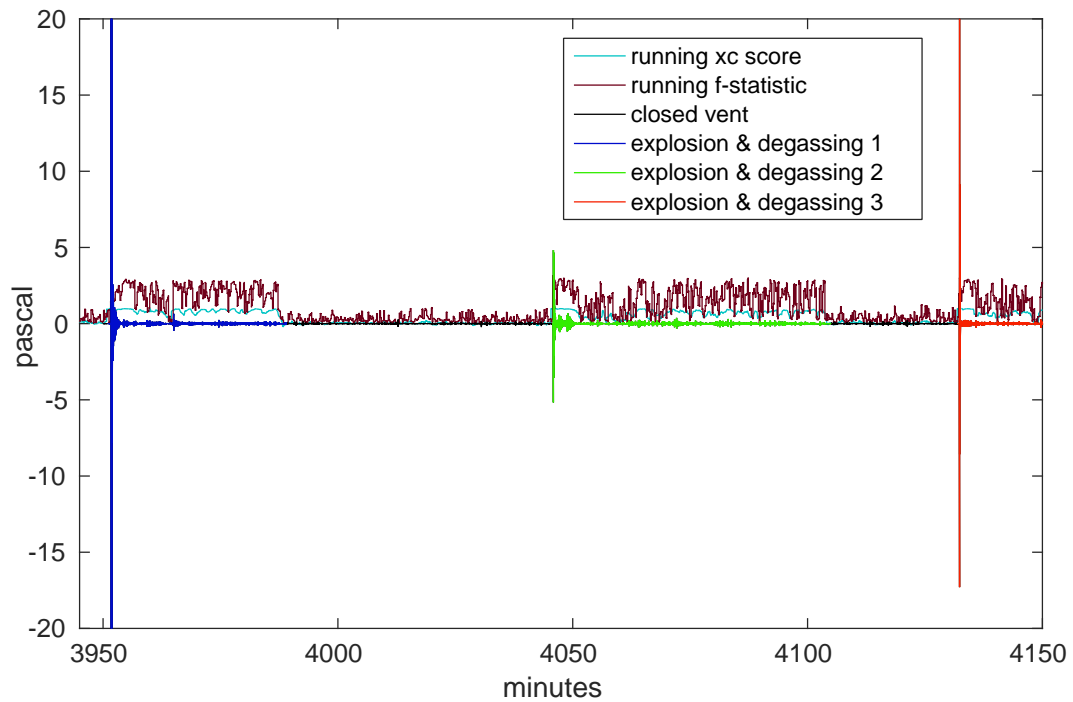
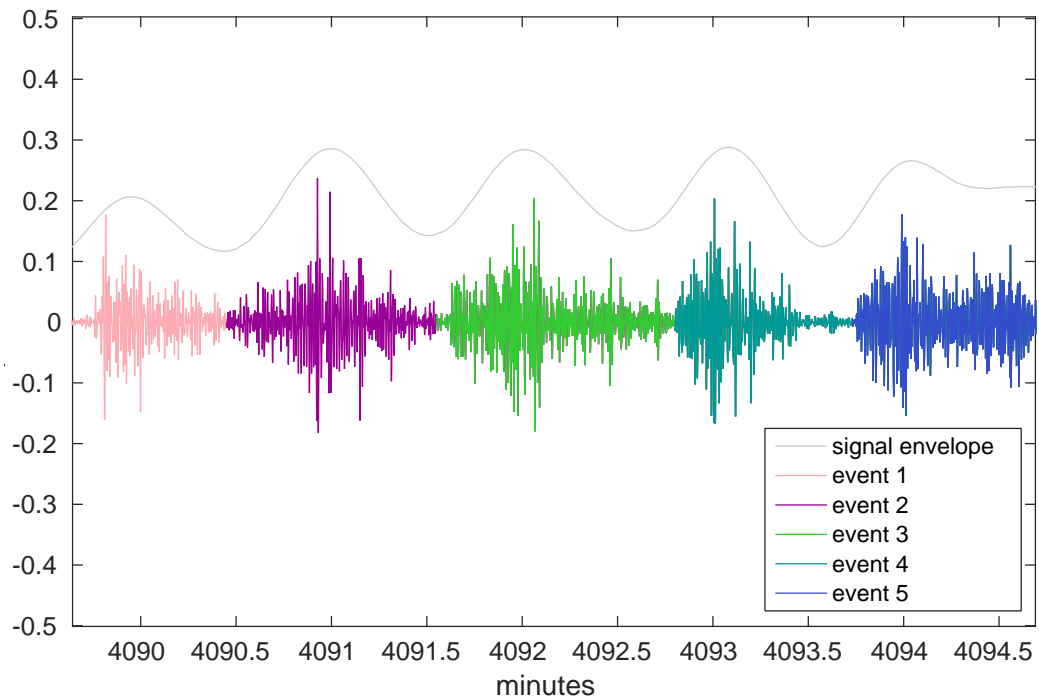


Figure 2.8: Three explosion events followed by degassing are identifiable from both signal cross-correlation and calculation of the Fisher statistic. Each explosion is preceded by the absence of detectable acoustic signal. Infrasonic waveforms are plotted in excess pressure (Pa), running normalized cross-correlation scores range  $(-1, 1)$ , and the Fisher statistic is plotted on a  $\log_e$  scale.



**Figure 2.9:** A close up of the second explosion tail in Figure 2.8 shows very short duration, low amplitude, discrete events; this study regards transient signals such as these as one single open-vent occurrence, as it is unclear in the coherency scores of any loss of signal; the F statistic remains elevated.

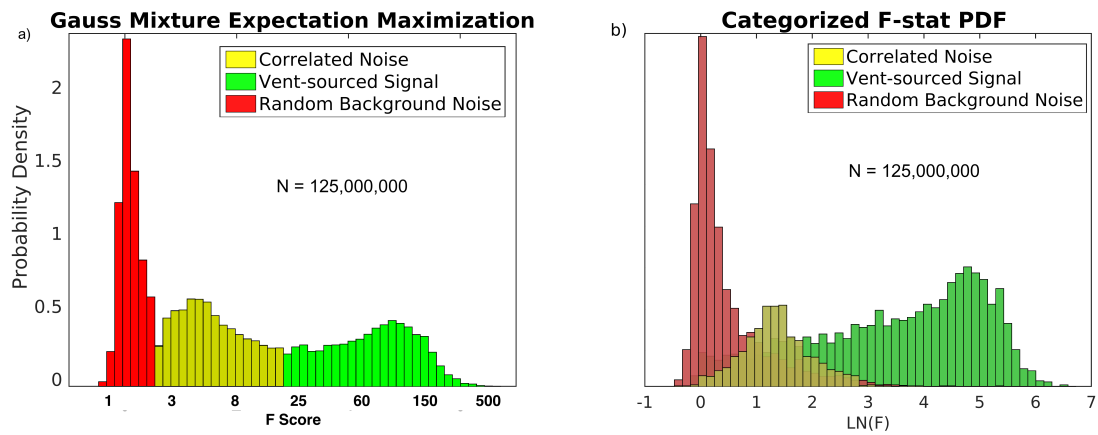


Figure 2.10: On the left is an idealized F statistic categorization method using hard cutoff values; while on the right, values are placed in temporal context.

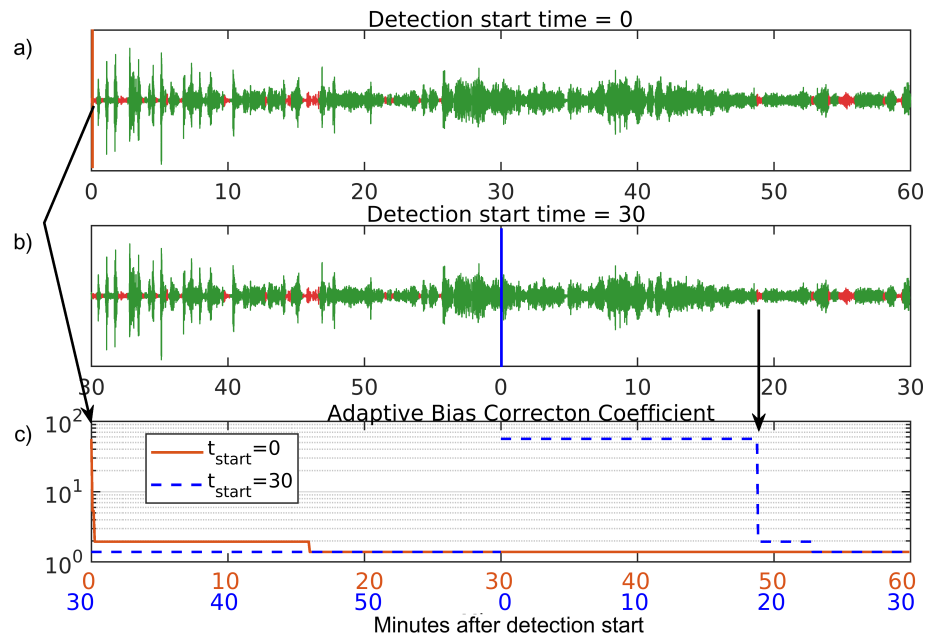


Figure 2.11: A randomly selected hour of infrasound is shown as a time series in panels a) and b). In panel a), the detection algorithm starts at time zero and moves through the hour at 15 seconds intervals. Panel b) shows the same infrasound time series, but the detection algorithm starts 30 minutes in and loops back through the beginning. Panel c) shows the Adaptive Bias Correction Coefficient (ABCC) value. Black arrows illustrate the first loss of coherent volcano-sourced infrasound seen by the detection algorithm.

## 2.4 Discussion

Observed in the F statistic distributions calculated independently for each array are slight translations of both the peak associated with clutter, and the peak representative of volcanic infrasound produced from the vent at Showa Crater. I propose that site location is responsible for the variations observed between the two F statistic distributions (Figure 2.12). One of the goals in mind during this week-long infrasound deployment was to observe the effects of topography on volcano infrasound; the two arrays used in this study differ in their placement such that local topographic effects can be observed.

Microphones at array KUR are situated on the Eastern flank of Sakurajima with line of sight to Showa Crater rim, while array HAR is located on the Western flank of Sakurajima on the leeward side of significant topography from Showa Crater. This difference in site topography is evident as a shift of the F scores produced from volcanic infrasound signal about the abscissa. The F statistic scores associated with volcanic infrasound signal are greater at array KUR than at array HAR. This means signal recorded on microphones at array KUR have a higher signal to noise ratio.

The background noise distribution is almost identically positioned at both arrays, but the two higher-scoring peaks (denoting clutter and volcanogenic infrasound, respectively) in the F statistic distributions are positioned differently for each array (Fig. 2.12). Clutter is more coherent at array HAR, while calculated F statistics of vent-sourced infrasound do not score as high at array HAR compared to array KUR. I draw two conclusions from these observations:

- Volcano-sourced infrasound signal coherency scores are reduced at array HAR due to signal distortion from local topography.

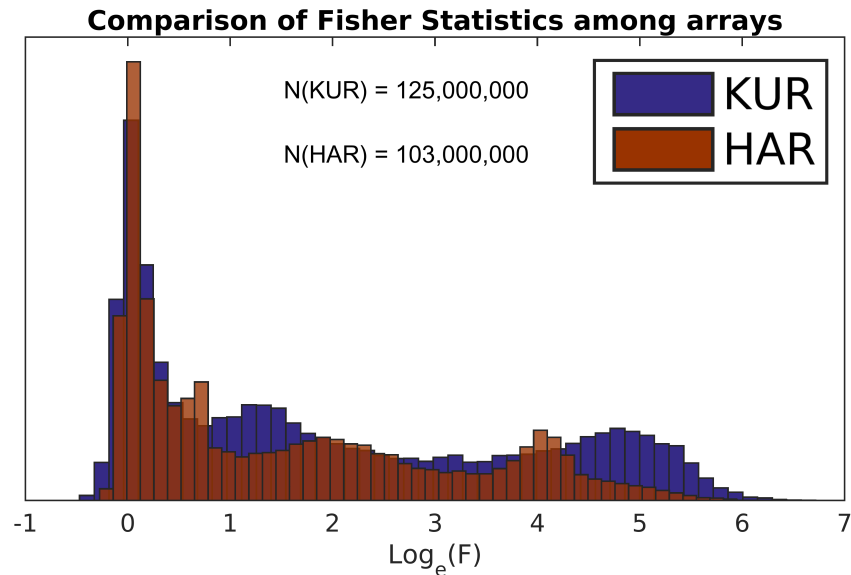


**Figure 2.12:** Calculated F statistics for both arrays shown as histograms. N is the number of samples used in each histogram.

- Clutter producing the central peak in each F score distribution is associated with anthropogenic noise from Kagoshima Bay.

## 2.5 Summary

From the previously described array processing methods, I obtain a time series record of volcanic infrasound activity that allows for quantitative categorization of eruptive behavior and temporal behavior analysis. I have shown how the Fisher statistic can be used as a statistic to differentiate a signal of interest from continuous background signal (clutter) and random noise. This technique may be valuable in scenarios where beamforming may fail, such as in the case where two signal generators share a common azimuth from a single array of sensors.

I use the maximum recorded pressure amplitudes of Sakurajima infrasound to categorize detections into either emergent, tremor-like degassing events ( $< 3.5$  Pa peak

amplitude, recorded) or explosive eruptions ( $> 3.5$  Pa peak amplitude, recorded). By sorting events into two categories, I calculate statistics independently for both types of activity for statistical eruption forecasting between event types.

Detection of coherent infrasound originating from the vent account for 54.4% of the acquisition duration as determined by using independent infrasound detections from arrays HAR and KUR. Explosive eruptions and associated degassing take up nearly one third of the total open-vent duration. Repose intervals (quiet periods where no infrasound is detected) range from 1 minute to approximately 6 hours in duration. Prior to all 28 detected explosions the absence of vent-sourced infrasound is observed at both arrays.

## **CHAPTER 3:**

# **INFRASOUND REPOSE INTERVAL DISTRIBUTION MODELING AND STATISTICAL EXPLOSION FORECASTING**

This chapter applies probabilistic modeling and forecasting methods to the volcanic infrasound characterized in the previous chapter. Probabilistic models parameterize the the likelihood of a random variable taking on a certain value based upon the distribution of past observed values; for example, the rate parameter of the Poisson probability distribution function controls the arrival rate of a random event. The statistical model used here describes the probability of observing an inter-event time (time from the end of one event to the beginning of another) in terms of the arrival rate. The arrival rate is a parameter of the Poisson distribution that describes the most probable number of events to be observed per unit time. Thus, parameterizing the distribution of repose intervals between recorded volcanic infrasound events can provide insight into how probable any number of events are to occur in a given time interval.

Statistical probability models that have been employed on the distribution of wait times between detected volcanic events include the exponential, Weibull, log-logistic, log-normal, and gamma probability models (Varley *et al.*, 2006). Each of

these distributions allow for different parameterization of volcano behavior. The single-parameter exponential distribution describes the rate at which the frequency of observed events decreases as event magnitude increases. The Weibull and gamma distributions are generalized versions of the exponential distribution and model non-stationary and stationary time series, respectively. The two parameter Weibull distribution (non-stationary process) can be used to describe whether probability of event occurrence increases or decreases as time after a previous event increases. The two parameter gamma distribution (stationary process) has been used to describe system failures as a function of time. Both distributions have been used to model volcano repose interval distributions.

Volcán de Colima (May 2002) and Karymsky (1997 and 1998) repose datasets have been modeled by Weibull distributions (Varley *et al.*, 2006). The Karymsky repose model has a shape parameter greater than one, representing a non-stationary process that has decreasing likelihood of event occurrence as time after a previous event increases (Varley *et al.*, 2006). The Volcán de Colima repose interval distribution model has a shape parameter less than one, representing a non-stationary process with increasing likelihood of event occurrence as time after a previous event increases. Volcán de Colima (June-July 2003, and March-September 2004) repose interval data were separated into two event types (explosive and degassing) that were best fit by a gamma distribution model. Furthermore, a daily average repose interval length at Colima over the six month period March-September 2004 was modeled as a log-logistic distribution (Varley *et al.*, 2006). This shows the sensitivity of statistical probability models on processed data.

Three statistical probability models (exponential, Weibull, and gamma) are used

to parameterize one week of infrasound data from Sakurajima. The data was processed and characterized previously as Chapter 2 of this thesis. During periods of persistent activity, such as the eruptive period from which the week long infrasound recordings represent at Showa Crater July 18-25, 2018, the wide range of volcanic behavior and structure of repose interval distribution of detected events can be used to statistically determine probable future repose interval durations.

I make assumptions necessary to model the week long record of volcanic activity at Sakurajima as a Poisson process (Table 3.1).

**Table 3.1: Poisson Assumptions**

Independence	The occurrence of an event does not change the probability of another event occurring.
Constant arrival rate	Over a long enough observation period, the number of events per unit time converges to a real value.
Sequentionation	Two events cannot occur at the exact same time.
Proportionality	The probability of an event occurring in an interval window is proportional to the window length.

Under these assumptions, the probability of observing any number of events can be modeled as a function of interval time  $\tau$ , number of events  $K$ , and intensity  $\lambda$  as

$$P(K) = \exp(-\lambda\tau) \frac{(\lambda\tau)^K}{K!} \quad \text{for } K = 1, \dots, n \quad (3.1)$$

This relation provides a quantitative statistical assessment of hazard (event) likelihood based on previous observations. A constraint of this distribution model is the discrete nature of  $K!$ , however, the gamma distribution model provides a continuous analog to the Poisson distribution

The gamma distribution model takes the form

$$P(X; \alpha, \beta) = \frac{\beta^\alpha x^{\alpha-1} e^{-\beta x}}{\Gamma(\alpha)} \quad \text{for } x, \alpha, \beta > 0 \quad (3.2)$$

where  $\alpha$  is the shape parameter,  $\beta$  is the rate parameter, and  $\Gamma$  is the gamma function evaluated at  $\alpha$ . A continuous distribution is necessary to model a continuous variable such as time. The gamma distribution is a two-parameter generalization of the exponential distribution. For  $\gamma = 1$  the gamma distribution reduces to the exponential distribution.

The Weibull probability distribution (3.3) is also a generalization of the exponential distribution.

$$P(X; k_w, \lambda) = \frac{k_w}{\lambda} \left(\frac{X}{\lambda}\right)^{k_w-1} e^{-(X/\lambda)^{k_w}} \quad \text{for } X, k_w, \lambda \geq 0 \quad (3.3)$$

Parameters  $k_w$  and  $\lambda$  are the shape and scale parameters, respectively. The Weibull distribution does not model a stationary process. Depending on the value of  $k_w$ , the rate at which events occur may either decrease over time ( $k_w < 1$ , promoting clustering of events), remain the same ( $k_w = 1$ ), or increase ( $k_w > 1$ ) as time after the last occurrence increases. Changing probability with time violates the independence of events required by the Poisson process. There is, however, evidence of explosion clustering in time (Fig. 3.1). Large explosion events seem to occur in groups of 1 to 7 individual explosions followed by a few hours of emergent degassing activity. This may be evidence that gas is not accumulating at a constant rate underneath a viscous rock cap over the study period, suggesting that the explosion process is non-stationary and best modeled with a Weibull distribution.

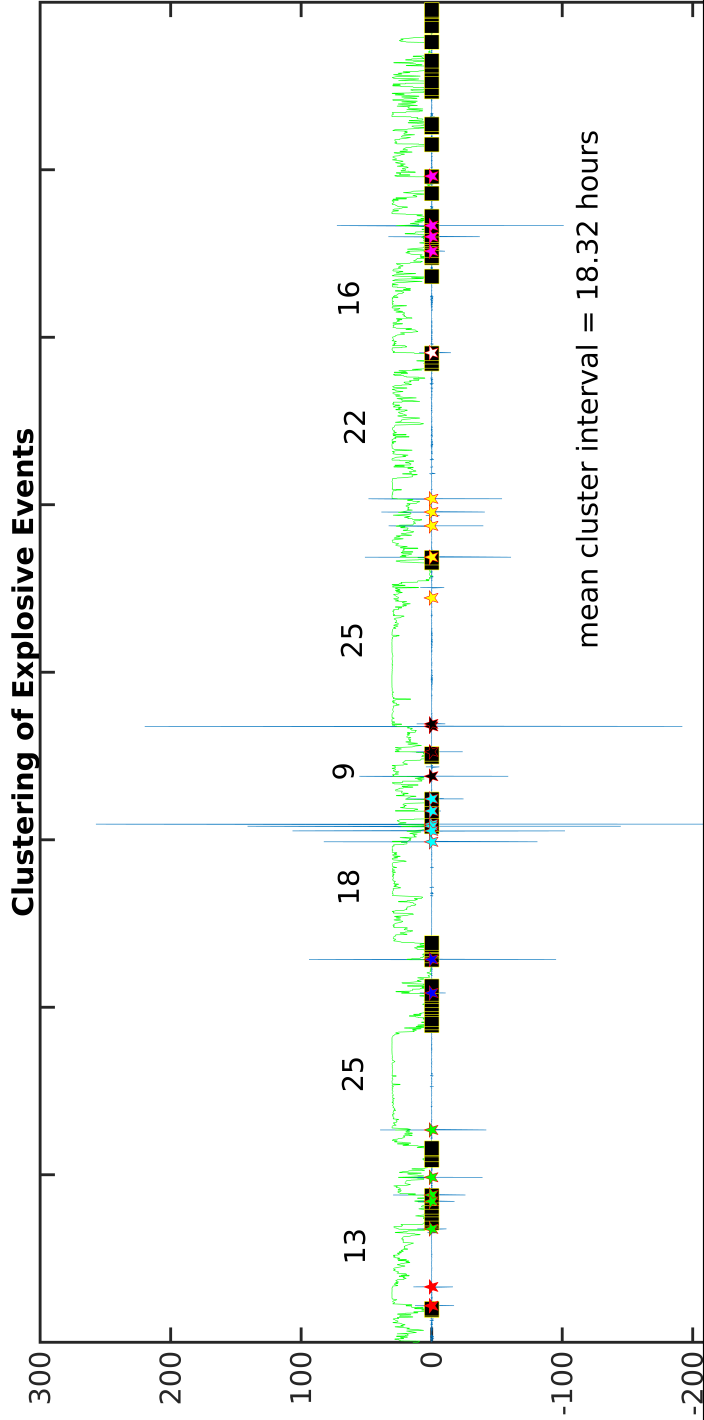


Figure 3.1: Infrasound beam-stack of recordings at array KUR display clustering of large amplitude explosions. Numbers represent time in hours between explosion cluster centers. Black boxes represent explosion forecasts based on loss of detected vent-sourced infrasound denoted by microphone cross-correlation scores.

## 3.1 Methods

### 3.1.1 Repose Interval Distribution Modeling

Various statistical models (gamma, Weibull, exponential, and log-logistic) have been used to fit volcano repose interval distributions. The wait-time between events have been best fit by these statistical models that describe a survival process, resulting from failure of some component over time, rather than a renewal process (Varley *et al.*, 2006). The two models that best fit the observed repose interval data at Sakurajima differ in the probability of observing an event as time passes. The gamma probability model describes a process that has uniform likelihood of occurrence in any time interval, and the occurrence of an event does not affect the probability of another the next event. Such a process is considered stationary. The Weibull probability model describes a process that becomes more or less likely to occur as time passes after an event has occurred, thus represents a non-stationary process.

Best fit models are sensitive to when, where, and how data is collected. For instance, seismic detection is typically not sensitive to the lower extremes of volcanogenic earthquakes, while historical eruptive history is limited by observable evidence. This means intermediate repose intervals and eruption events are statistically more likely to be observed, introducing bias into parameter estimation models. Continuous infrasound array monitoring at volcanoes has the potential to reduce these observational errors. However, for this dataset, I use a method of random sampling (Monte Carlo bootstrapping) the observed data many times to create a broader population of possible data subsets.

## Bootstrapping

Bootstrapping is a method of using a sample population to estimate parameters of the total population. Monte Carlo Bootstrapping is performed by repeatedly sampling subsets of the observed sample population. Each sub-population (realization) becomes its own sample population which is used to estimate the parameters of interest for an entire population. A normal distribution for each model parameter value is constructed after many iterations of random sampling. The mean of each normal distribution is used to describe the expected best fit for the entire population and the variance of each parameter distribution is used to assess confidence in the value.

Under Poisson assumptions, the underlying process is stationary and the arrival rate is fixed. For the week-long observation period, 366 transient infrasound events were detected. The estimated arrival rate is about 2 events per hour. Thus, the data is assumed to represent a dynamic range of the stochastic process, but is also assumed to be incomplete. Robust modeling of the repose interval distribution requires a comprehensive dataset. This is achieved by using the bootstrapping technique *method 2* of Efron (1979).

Since events are considered independent random variables, each realization may contain multiple instances of any observed data point (random sample with replacement). The Monte Carlo process aims to develop a suite of possible observable outcomes that act as an extension of the dataset. This method is validated by the stationary Poisson process assumption. The Poisson process over the period which data is used in modeling is considered to be constant, or stationary. Over long enough periods of time, volcanic behavior is often not constant. In this week-long study of eruptive activity at a single volcanic vent, it may be fair to assume that the controlling

process is rather constant, thus representing a stationary Poisson process.

### 3.1.2 Likelihood and Confidence

I employ two goodness-of-fit tests to help determine whether observed data come from a known distribution model, the Kolmogorov-Smirnov (KS) test and the Anderson-Darling (AD) test. The KS test (Eq: KS) is a non-parametric hypothesis test that tests two CDFs by calculating a test statistic,  $D^*$ , which is the maximum difference of the proportion ( $\hat{F}_1$  and  $\hat{F}_2$ ) of each cdf that is less than or equal to  $x$ , where  $x$  covers the range of data (Massey, 1951).

$$D^* = \max_x(\text{abs}(\hat{F}_1(x) - \hat{F}_2(x))) \quad (3.4)$$

The Anderson-Darling test (Eq: AD) is more sensitive the the tail ends of each distribution (Anderson & Darling, 1952). This test uses a weighting function  $w(x) = [F(x)(1 - F(x))]^{-1}$  to penalize departures from the distribution model at both tails. The test statistic takes the form

$$A = n \int_{-inf}^{inf} (F_n(x) - F(x))^2 w(x) dF(x) \quad (3.5)$$

Varley *et al.* (2006) used these two tests to assess statistical models of volcano repose interval distributions at various volcanoes and found that log-logistic, gamma, exponential, and Weibull distribution models were able to explain the observed distributions. The gamma and Weibull distribution models were not rejected by either test for the repose interval data used in this study; computed test statistics for each model and their significance level are given in Table (3.2). Distribution model fit results are shown in Figure 3.2.

**Table 3.2: Goodness-of-fit Hypothesis Testing**

Distribution Model	KS test	AD test
Gamma	0.228 (0.001)	5.330 (0.005)
Weibull	0.236 (0.001)	6.044 (0.001)

Test statistic results are accompanied by the significance level in parentheses.

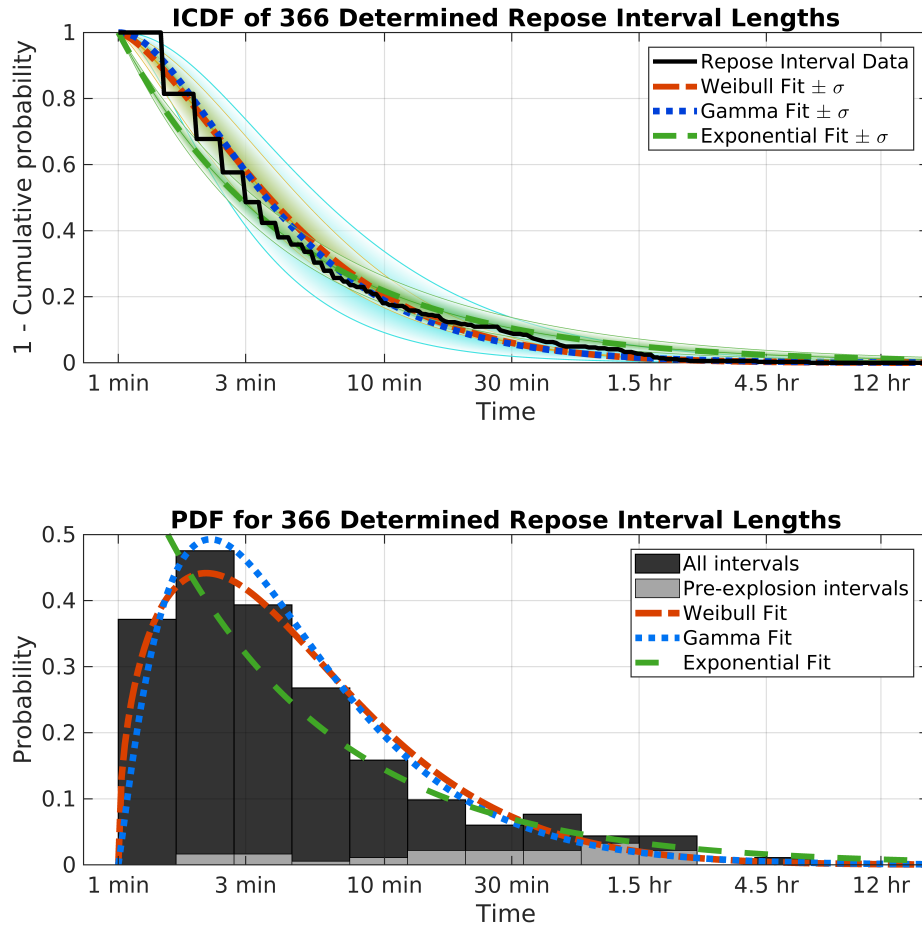


Figure 3.2: Weibull (orange), Gamma (blue), and Exponential (green) probability distributions are fit to the repose interval data (black line). (a) Empirical survival curve from data fitted with exponential and gamma cdfs; shaded areas represent uncertainty out to  $\sigma$  (95% confidence) uncertainty is estimated from the variance of  $\mu$  and  $\sigma$  distributions produced from 1000 Monte Carlo fits to a randomly selected 75% of the data. (b) All repose intervals (black histogram) are compared with only the repose intervals ending in explosion (grey histogram).

## 3.2 Results

### 3.2.1 Probabilistic Explosion Forecasting

During the eruption sequence, or sustained period of high activity level, observed the week of July 18-25, 2013 at Sakurajima Volcano, the relationship between vent-sealing and explosive eruption is quantified and compared to non-explosive degassing events. It is apparent in the results that long quiescent periods are more likely to result in an explosive eruption (Fig 3.2).

Infrasound detection results at Sakurajima show correlation between quiescence time duration and the type of activity at the vent (i.e. longer repose intervals are more likely to result in explosions while shorter repose intervals most often lead to emergent, tremor-like degassing events). Explosion likelihood is calculated from the ratio of the survival functions of repose intervals leading up to explosions and the survival of repose intervals resulting in passive degassing events (Fig 3.3).

### 3.2.2 Near-real-time Application

Cataloging events to build a statistical model is the basis of event forecasting. Benefits increase if the method can be applied in real-time. Sakurajima volcano displays a range of eruptive behavior; variations between the pre-eruptive observations (such as vent closure time) are used to determine which type of event is most likely to occur given the current status (of observed closure time).

Detected events are autonomously categorized as either explosions or emergent, degassing events based on maximum recorded amplitude. Explosions commonly extend one or more orders of magnitude in maximum pressure amplitude ( $Pa$ ) beyond emergent, non-explosive, events thus differentiation based on amplitude is quite ac-

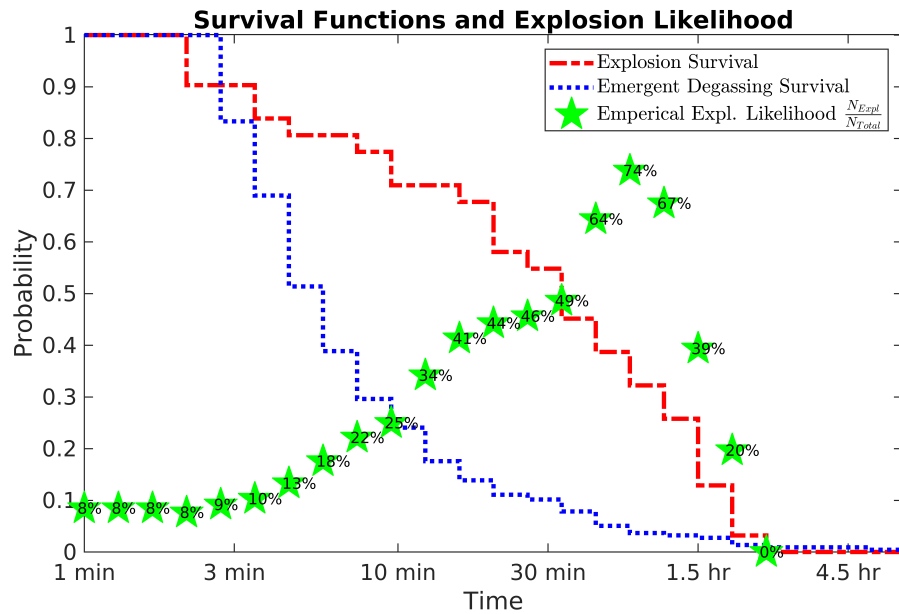


**Figure 3.3:** Survival functions for observed repose intervals resulting in explosions (*red*) and emergent degassing events (*blue*). Green stars show the observed percentage of explosions relative to the total number of events that share similar repose interval times; note the logarithmically increasing bin sizes for repose interval time. Explosion likelihood increases significantly after about 45 minutes of infrasonic quiescence.

curate (Fig. 3.7).

Assuming deterministic (can be modeled by a single probability model throughout) eruptive behavior, I use previously observed interval times and their resulting eruption style to construct closure time distributions associated with both styles of eruptive activity at Sakurajima. Since these distribution models are likely unknown at many volcanoes and closure time can span multiple orders of magnitude (seconds to hours), I use the median ( $\bar{\mu}_N$ ,  $\bar{\mu}_X$ ) of each distribution to describe the distribution of closure times that result in non-explosive and explosive activity, respectively. Error between the current closure time and each distribution median is used as an explosion

forecasting variable. This function takes the form

$$RSMRS_X(L) = \sum \left( \frac{n_X}{n_N} \cdot \frac{\bar{\mu}_N - L}{\bar{\mu}_X - L} \right)^2 \quad (3.6)$$

The Relative Squared Median Residual Sum ( $RSMRS_X$ ) is a quantitative measure of how likely a future event is to be explosive based on the distributions of prior observations of quiescence preceding detected explosions and non-explosions. The values  $\bar{\mu}_X$  and  $\bar{\mu}_N$  are the medians of repose interval times that precede explosions (denoted by subscript  $X$ ) and non-explosions (denoted by subscript  $N$ ), respectively; these median values are compared with observed repose interval time length ( $L$ ) in near-real-time. The  $RSMRS_X$  ranges from zero to infinity and is best visualized on a logarithmic scale. Since small values are produced when the numerator is very small or the denominator is very large, values near zero suggest that the next event will likely be non-explosive. This occurs when the observed repose time is either close to the non-explosive median repose time, or not close to the explosive median repose time length. Alternatively, high values of  $RSMRS_X$  indicate a higher probability of an explosive event, based on past behavior.

The range of  $RSMRS_X$  values is infinite, thus the values do not represent absolute probability of observing either type of eruptive behavior; to be useful for event style forecasting, distributions of repose intervals for each event type must be distinguishable from one another. Such as with signal detection using the Fisher statistic the distributions may overlap or share other similarities, but each event type is expected to converge on a respective arrival rate that I assume can be characterized by the median repose interval time; the median is a robust statistic for comparing distributions that range over multiple orders of magnitude. The forecasting variable contains a

normalization coefficient,  $\frac{n_X}{n_N}$ , which accounts for the number of each observed event type;  $n_X$  is the number of observed explosions and  $n_N$  is the number of observed non-explosions. Since statistical forecasting is based on information gathered from previously observed activity, this normalization coefficient favors the more frequently observed style of activity.

The value of  $RSMRS_X$  does not have a physical meaning and must be interpreted based on two parameters: 1) the peakedness of each distribution, which can be considered analogous to the variance for this application, and 2) the separation of the distributions relative to each other. After a set of initial observations has been made, an arbitrary value can be chosen to discriminate between whether an explosive or non-explosive event is more likely to occur (Fig 3.4; Fig 3.5).

A Receiver Operating Characteristic (ROC) curve (Fig 3.6) is constructed for explosion predictions and is used to assess a proper cutoff value. The cutoff value should depend heavily upon whether or not the volcanic system displays deterministic behavior, or whether each event type shows a preferred closure time that is distinct from the other, such as is observed at Sakurajima over the study period. The large area underneath the ROC curve suggests that the RSMRS is a good forecasting variable (Zhang *et al.*, 2016). Efficiency and effectiveness of the forecaster are based on probability of false positive detection versus probability of true positive detection. There are two cutoff values that present similar results in terms of area, however each offers advantages and disadvantages. Table 3.2 displays these values and their corresponding detection probabilities.

However, the cutoff 0.2998 maximizes the ratio of true positive predictions to false positive predictions which ultimately is more important when dealing with eruption

**Table 3.3: Forecasting Probability Cutoff Values & Statistics**

Cutoff	$P_{TP}$	$P_{FP}$	Acc.	Prec.
0.2998	92.86%	15.48%	85.04%	28.52%
0.3374	89.3%	52.8%	87.28%	31.17%

hazards (Tab 3.3). The fact that there are overwhelmingly more non-explosive events biases the ROC results towards discounting the number of false positives relative to true positives.

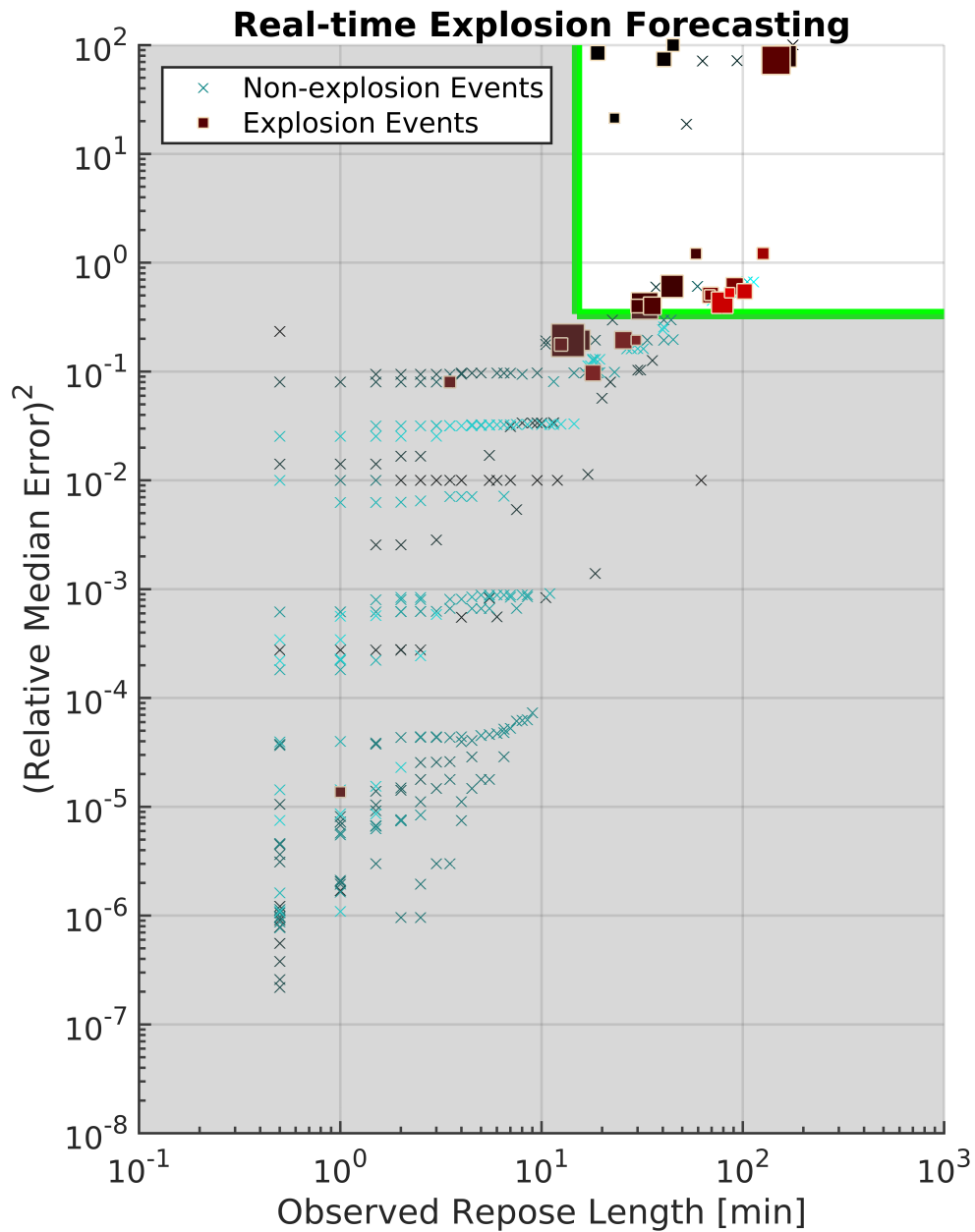


Figure 3.4: The square of the relative error between each distribution median and the current observed repose interval is used as an objective function to predict explosion probability. The green boxed area represents the area where the observed repose interval is predicted to result in explosive activity using 0.2998 as a cutoff.

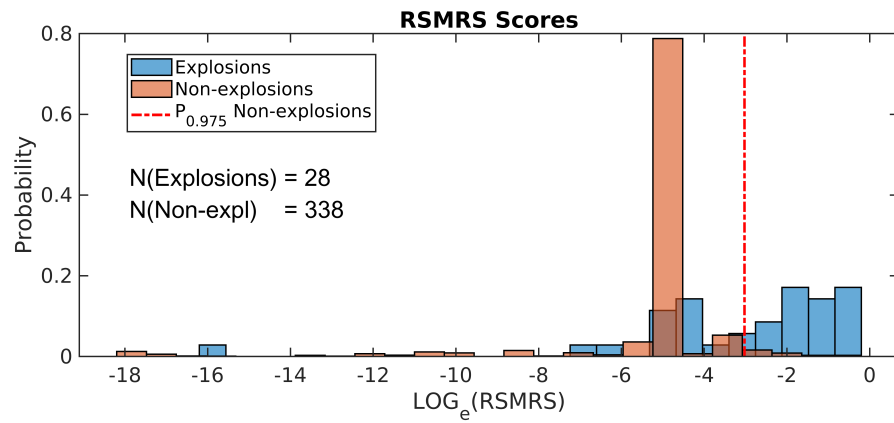


Figure 3.5: Probability density function shows calculated RSMRS values prior to each detected infrasound event. The blue bars are for detected explosions and orange bars are for non-explosive degassing events; the red dashed line marks a cutoff value that separates 97.5% of non-explosions from 74% of explosions.

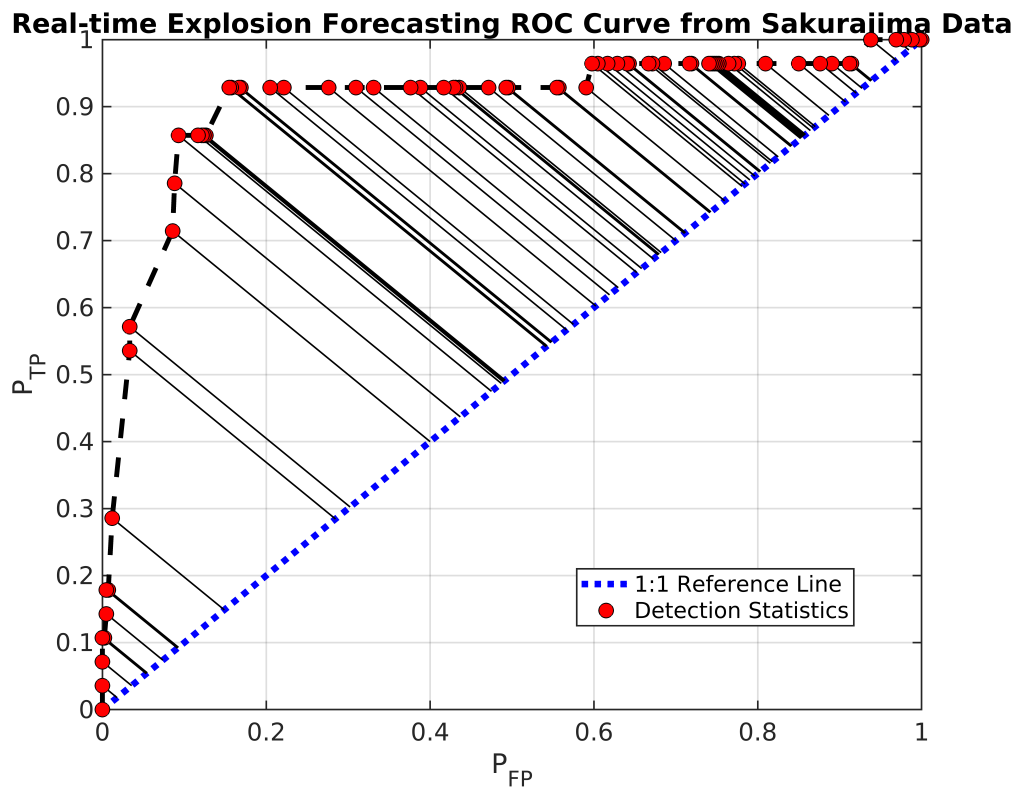


Figure 3.6: Receiver Operating Characteristic (ROC) curve displaying explosion forecasting results from July 18-25 at Sakurajima Volcano using the RSMRS forecasting variable at various cut-offs.

## 3.3 Discussion

### 3.3.1 Sakurajima

At the onset of this research project, I expected to find a positive correlation between the repose interval duration and the resulting explosion amplitude, however, analysis of infrasound detections reveals there is no clear relationship between quiescence time and recorded explosion amplitude (Fig. 3.7).

The study observation period was very short (1 week), and the amount of explosions (28 recorded on both arrays) used in this study do not allow for robust statistical comparison of outlier events. This, in conjunction with incoherent (wind) noise and correlated noise across each array during much of the recording period introduce uncertainty in determination of whether the vent at Showa crater is sealed or not prior to all explosions, however, analysis suggests that there is an absence of vent-sourced infrasound prior to explosions.

Non-explosive degassing at Sakurajima produces a lower amplitude signal than explosive eruptions. Coincidentally, the majority of short-duration repose intervals are observed between emergent degassing events. Low-amplitude signal from the vent is susceptible to interruption from wind (and other) noise. I used band-pass filtering and beam-stacking to reduce the effect of wind on degassing signals, however, the effect remains apparent in the results and may account for the short duration repose intervals associated with many low amplitude degassing events.

### 3.3.2 Physical Processes

Characterization of the frequency at which volcanic events operate is important for estimating timescales and rates of subsurface processes that drive eruptions, as

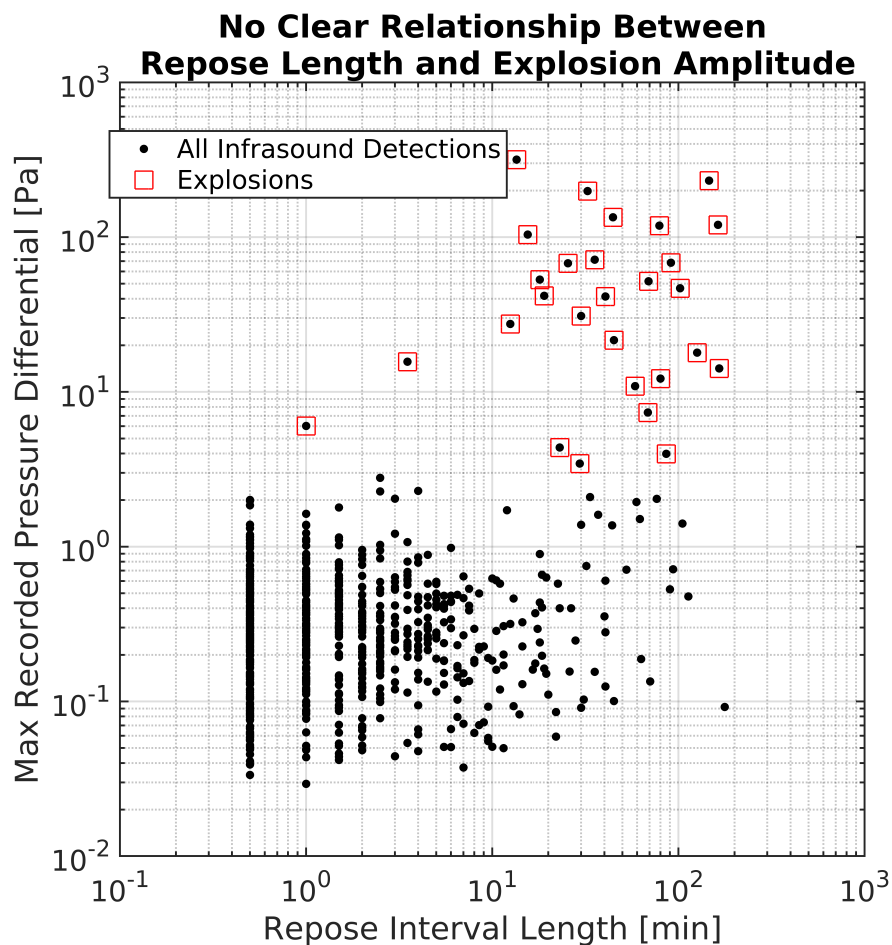


Figure 3.7: Explosions are separated based on both recorded pressure amplitude and quiescent time leading up to the event. Explosions are outlined by red boxes.

well as for understanding the statistical likelihood of encountering an explosion during periods of sustained unrest.

A number of studies suggest Vulcanian eruptions are a result of material failure (Woods, 1995; Connor *et al.*, 2003). Activity at Volcan de Colima, which exhibits similar behavior to Sakurajima Volcano, has been modeled as a material failure phenomenon (De la Cruz-Reyna & Reyes-Dávila, 2001). Varley *et al.* (2006) found that

for different periods of activity in 2002, both Weibull and gamma distribution models describe volcanic repose interval durations at Colima. I have obtained a gamma best fit model for the observed repose interval durations at Sakurajima during 18-25 July 2013. Infrasound data used in a study by Uhira & Takeo (1994) showed a clear inflationary phase just prior to the onset of each eruption at Sakurajima. I support the claims of Michaut *et al.* (2013) and Cassidy *et al.* (2015), in that the observed inflation may be an observation of gas accumulating inside the conduit immediately prior to material failure of a viscous cap, leading to explosion onset.

Explosions appear to be clustered in time. Kmeans clustering algorithm separated out 8 clusters with a mean 18.32 hour interval between cluster centers. Kmeans takes an input of maximum number of clusters to assign while minimizing the distances from the cluster means.

### 3.4 Conclusion

In Chapter 2 I have developed a strategy to identify when a particular volcanic vent is openly emitting infrasound. From this analysis I obtain a time series record of open vent activity as well periods of no detectable signal above the background infrasound noise level. Although background noise Fisher statistics are elevated from the presence of clutter, according to Wirth *et al.* (1971) low amplitude signal from Showa Crater would still be detectable given the observed SNR, thus I determine the vent to be closed (not degassing) during detected quiet periods longer than the minimal 1 minute. This analysis allows for precise distribution modeling and statistical forecasting of repose interval durations.

In Chapter 3 I have shown that infrasound repose interval times at Showa Crater may be modeled as a Poisson process with a gamma probability distribution over

the week long recording period. Furthermore, repose interval time can be used as a predictor variable for explosive Vulcanian eruptions at Sakurajima during periods of sustained volcanic unrest. This analysis may be applicable to other silicic volcanic systems that exhibit intermittent activity. At Showa Crater, the single-variable forecasting algorithm operates with a true detection rate of 93% and a false positive rate of 15%. Although this might seem like an ideal forecaster, the large number of non-explosive events drives down the false positive percentage. If we examine the ratio of true positives to predicted positives, the forecaster operates with 72% of predicted explosions ending in non-explosive behavior.

Arguably, at Sakurajima Volcano, a 72% false alarm rate is acceptable. The main danger associated with these small explosive eruptions are ejecta and small ash clouds that can affect nearby tourists and aircraft. However, this false alarm rate is problematic if extensive societal disruption occurs for nearby communities in anticipation of explosive eruption. Closing public areas and relocating people costs time, effort, and money. These more drastic measures would not work feasibly with such a high false alarm rate. Furthermore, any institution that uses a zero risk policy approach may suffer from this forecasting attempt.

Fortunately, the false alarm rate can be reduced at the cost of training the algorithm with a few hours of data prior to forecasting. The ABCC converges after a few minutes of observed background (determined from theoretical Fisher statistics). Discarding forecasting results until after the ABCC has converged yields only a 26% false alarm rate for the rest of the entire dataset (147 hours).

## REFERENCES

- Abramowitz, Milton, & Stegun, Irene A. 1972. Handbook of Mathematical Functions with Formulas, Graphs, and Mathematical Tables. *National Bureau of Standards*, 1076.
- Alatorre-Ibargüengoitia, Miguel A., Scheu, Bettina, & Dingwell, Donald B. 2011. Influence of the fragmentation process on the dynamics of Vulcanian eruptions: An experimental approach. *Earth and Planetary Science Letters*, **302**(1-2), 51–59. doi:10.1016/j.epsl.2010.11.045.
- Anderson, Jacob F., Johnson, Jeffrey B., Bowman, Daniel C., & Ronan, Timothy J. 2018. The Gem Infrasound Logger and CustomBuilt Instrumentation. *Seismological Research Letters*, **89**(1), 153–164. doi:10.1785/0220170067.
- Anderson, T W, & Darling, D A. 1952. Asymptotic theory of certain "goodness-of-fit" criteria based on stochastic processes. *Annals of Mathematical Statistics*, **23**, 193–212. doi:10.1214/aoms/1177729437.
- Arrowsmith, Stephen J., Whitaker, Rod, Katz, Charles, & Hayward, Chris. 2009. The F-detector revisited: An improved strategy for signal detection at seismic and infrasound arrays. *Bulletin of the Seismological Society of America*, **99**(1), 449–453. doi:10.1785/0120080180.
- Blandford, R R. 1974. An automated event detector at the Tonto Forest Seismic Observatory. *Geophysics*, **39**(5), 633–643.
- Booker, Aaron, & Backus, Milo M. 1965. Matrix-multiply Detection Processing of Array Data. *Array Research Preliminary Report (No. SR-8)*.
- Cassidy, Mike, Cole, Paul D, Hicks, Kelby E, Varley, Nick R, & Peters, Nial. 2015. Rapid and slow: Varying magma ascent rates as a mechanism for Vulcanian explosions. *Earth and Planetary Science Letters*, **420**(June), 73–84. doi:10.1016/J.EPSL.2015.03.025.
- Connor, C. B., Sparks, R. S. J., Mason, R. M., Bonadonna, C., & Young, S. R. 2003. Exploring links between physical and probabilistic models of volcanic eruptions: The Soufrière Hills Volcano, Montserrat. *Geophysical Research Letters*, **30**(13). doi:10.1029/2003GL017384.

- De la Cruz-Reyna, Servando, & Reyes-Dávila, Gabriel A. 2001. A model to describe precursory material-failure phenomena: applications to short-term forecasting at colima volcano, Mexico. *Bulletin of Volcanology*, **63**(5), 297–308. doi:10.1007/s004450100152.
- Denlinger, Roger P., & Hoblitt, Richard P. 1999. Cyclic eruptive behavior of silicic volcanoes. *Geology*, **27**(5), 459–462.
- Douze, E J, & Laster, S J. 1979. Short Note Statistics of semblance. *Geophysics*, **44**(12), 1999–2003.
- Efron, B. 1979. Bootstrap Methods : Another Look at the Jackknife. *The Annals of Statistics*, **7**(1), 1–26.
- Fee, D., Yokoo, A., & Johnson, J. B. 2014. Introduction to an Open Community Infrasound Dataset from the Actively Erupting Sakurajima Volcano, Japan. *Seismological Research Letters*. doi:10.1785/0220140051.
- Fisher, R A, Corbet, A Steven, & Williams, C B. 1943. The Relation Between the Number of Species and the Number of Individuals in a Random Sample of an Animal Population. *Source: The Journal of Animal Ecology*, **12**(1), 42–58.
- Garces, Milton A. 2000. Infrasonic signals generated by volcanic eruptions. *In Geoscience and Remote Sensing Symposium, 2000. IEEE 2000 International*, **3**, 1189–1191.
- Ichihara, Mie, Lyons, John J, & Yokoo, Akihiko. 2013. Switching from seismic to seismo-acoustic harmonic tremor at a transition of eruptive activity during the Shinmoe-dake 2011 eruption. *Earth Planets Space*, **65**, 633–643. doi:10.5047/eps.2013.05.003.
- Iguchi, Masato, Yakiwara, Hiroshi, Tameguri, Takeshi, Hendrasto, Muhamad, & ichi Hirabayashi, Jun. 2008. Mechanism of explosive eruption revealed by geophysical observations at the Sakurajima, Suwanosejima and Semeru volcanoes. *Journal of Volcanology and Geothermal Research*, **178**, 1–9. doi:10.1016/j.jvolgeores.2007.10.010.
- Iguchi, Masato, Tameguri, Takeshi, Ohta, Yusaku, Ueki, Sadato, & Nakao, Shigeru. 2013. Characteristics of Volcanic Activity at Sakurajima Volcanos Showa Crater During the Period 2006 to 2011. *Article Bull. Volcanol. Soc. Japan*, **58**(1), 115–135. doi:10.18940/kazan.58.1\_15.
- Ishihara, K. 1985. Dynamical analysis of volcanic explosion. *Journal of Geodynamics*, **3**(3-4), 327–349. doi:10.1016/0264-3707(85)90041-9.

- Johnson, J. B., & Miller, A. J. C. 2014. Application of the Monopole Source to Quantify Explosive Flux during Vulcanian Explosions at Sakurajima Volcano (Japan). *Seismological Research Letters*. doi:10.1785/0220140058.
- Johnson, Jeffrey B. 2004. Source location variability and volcanic vent mapping with a small-aperture infrasound array at Stromboli Volcano, Italy. *Bulletin of Volcanology*, **67**, 1–14. doi:10.1007/s00445-004-0356-8.
- Johnson, Jeffrey B., Aster, Richard C., & Kyle, Philip R. 2004. Volcanic eruptions observed with infrasound. *Geophysical Research Letters*, **31**, L14604. doi:10.1029/2004GL020020.
- Kanamori, Hiroo, Given, Jeffrey W., & Lay, Thorne. 1984. Analysis of seismic body waves excited by the Mount St. Helens eruption of May 18, 1980. *Journal of Geophysical Research*, **89**(10), 1856–1866. doi:10.1029/JB089iB03p01856.
- Kawakatsu, Hitoshi, Ohminato, Takao, Ito, Hisao, Kuwahara, Yasuto, Kato, Takashi, Tsuruga, Kayoko, Honda, Satoru, & Yomogida, Kiyoshi. 1992. Broadband seismic observation at the Sakurajima Volcano, Japan. *Geophysical Research Letters*, **19**(19), 1959–1962. doi:10.1029/92GL01964.
- Kim, Keehoon, & Lees, Jonathan M. 2014. Local Volcano Infrasound and Source Localization Investigated by 3D Simulation. *Seismological Research Letters*, **85**(6), 1177–1186. doi:10.1785/0220140029.
- Lyons, John J., Haney, Matthew M., Werner, Cynthia, Kelly, Peter, Patrick, Matthew, Kern, Christoph, & Trusdell, Frank. 2016. Long period seismicity and very long period infrasound driven by shallow magmatic degassing at Mount Pagan, Mariana Islands. *Journal of Geophysical Research B: Solid Earth*, **121**(1), 188–209. doi:10.1002/2015JB012490.
- Marcillo, Omar, Johnson, Jeffrey B., & Hart, Darren. 2012. Implementation, Characterization, and Evaluation of an Inexpensive Low-Power Low-Noise Infrasound Sensor Based on a Micromachined Differential Pressure Transducer and a Mechanical Filter. *Journal of Atmospheric and Oceanic Technology*, **29**(9), 1275–1284. doi:10.1175/JTECH-D-11-00101.1.
- Massey, F J. 1951. The Kolmogorov-Smirnov Test for Goodness of Fit. *Journal of the American Statistical Association*, **46**(253), 68–78.
- Matoza, R. S., Fee, D., & Lopez, T. M. 2014. Acoustic Characterization of Explosion Complexity at Sakurajima, Karymsky, and Tungurahua Volcanoes. *Seismological Research Letters*. doi:10.1785/0220140110.

- Matoza, Robin S., Fee, David, Green, David N., Le Pichon, Alexis, Vergoz, Julien, Haney, Matthew M., Mikesell, T. Dylan, Franco, Luis, Valderrama, O. Alberto, Kelley, Megan R., McKee, Kathleen, & Ceranna, Lars. 2018. Local, Regional, and Remote Seismo-acoustic Observations of the April 2015 VEI 4 Eruption of Calbuco Volcano, Chile. *Journal of Geophysical Research: Solid Earth*, **123**(5), 3814–3827. doi:10.1002/2017JB015182.
- Mckee, Kathleen, Fee, David, Rowell, Colin, & Yokoo, Akihiko. 2014. Network-Based Evaluation of the Infrasonic Source Location at Sakurajima Volcano, Japan. *Seismological Research Letters*, **85**(6), 1200–1211. doi:10.1785/0220140119.
- Melton, Ben S., & Bailey, Leslie F. 1957. Multiple Signal Correlators. *Geophysics*, **22**(3), 565. doi:10.1190/1.1438390.
- Michaut, Chloé, Ricard, Yanick, Bercovici, David, & Sparks, R. Steve J. 2013. Eruption cyclicality at silicic volcanoes potentially caused by magmatic gas waves. *Nature Geoscience*, **6**(10), 856–860. doi:10.1038/ngeo1928.
- Miwa, T., & Toramaru, A. 2013. Conduit process in vulcanian eruptions at Sakurajima volcano, Japan: Inference from comparison of volcanic ash with pressure wave and seismic data. *Bulletin of Volcanology*, 75:685. doi:10.1007/s00445-012-0685-y.
- Morrissey, M., Garces, M., Ishihara, K., & Iguchi, M. 2008. Analysis of infrasonic and seismic events related to the 1998 Vulcanian eruption at Sakurajima. *Journal of Volcanology and Geothermal Research*, **175**, 315–324. doi:10.1016/j.jvolgeores.2008.03.008.
- Ripepe, Maurizio, Marchetti, Emanuele, & Olivieri, Giacomo. 2007. Infrasonic monitoring at Stromboli volcano during the 2003 effusive eruption: Insights on the explosive and degassing process of an open conduit system. *Journal of Geophysical Research: Solid Earth*, **112**(B9). doi:10.1029/2006JB004613.
- Ripepe, Maurizio, Donne, Dario Delle, Genco, Riccardo, Maggio, Giuseppe, Pistolesi, Marco, Marchetti, Emanuele, Lacanna, Giorgio, Olivieri, Giacomo, & Poggi, Pasquale. 2015. Volcano seismicity and ground deformation unveil the gravity-driven magma discharge dynamics of a volcanic eruption. *Nature Communications*, **6**. doi:10.1038/ncomms7998.
- Rost, Sebastian, & Thomas, Christine. 2002. Array seismology: Methods and applications. *Reviews of Geophysics*, **40**(3), 1008. doi:10.1029/2000RG000100.

- Sanderson, R. W., Johnson, J. B., & Lees, J. M. 2010. Ultra-long period seismic signals and cyclic deflation coincident with eruptions at Santiaguito volcano, Guatemala. *Journal of Volcanology and Geothermal Research*, **198**(1-2), 35–44. doi:10.1016/j.jvolgeores.2010.08.007.
- Shumway, Robert H. 1971. On detecting a signal in n stationarily correlated noise series. *Technometrics*, **13**(3), 499–519. doi:10.1080/00401706.1971.10488814.
- Uhira, Kohichi, & Takeo, Minoru. 1994. The source of explosive eruptions of Sakurajima volcano, Japan. *Journal of Geophysical Research*, **99789**(10), 775–17. doi:10.1029/94JB00990.
- Varley, Nick, Johnson, Jeffrey, Ruiz, Mario, Reyes, Gabriel, & Martin, Kristin. 2006. Applying Statistical Analysis to Understanding the Dynamics of Volcanic Explosions. *H.M. Mader, S.G. Coles, C.B. Connor, L.J. Connor (Eds.), Statistics in Volcanology, Special Publication of IAVCEI, Geological Society, London (2006)*, 57–76.
- Venzke, E. 2015. Global Volcanism Program, 2015. Report on Aira (Japan). *Bulletin of the Global Volcanism Network*, **40**(11).
- Wirth, M H, Blandford, R R, & Shumway, R H. 1971. Automatic network detection. No. *SDL-285. Teledyne Geotech Alexandria VA, Seismic Data Lab.*
- Woods, Andrew W. 1995. A model of vulcanian explosions. *Nuclear Engineering and Design*, **155**(1-2), 345–357. doi:10.1016/0029-5493(94)00881-X.
- Yokoo, A., Suzuki, Y. J., & Iguchi, M. 2014. Dual Infrasonic Sources from a Vulcanian Eruption of Sakurajima Volcano Inferred from Cross-Array Observation. *Seismological Research Letters*. doi:10.1785/0220140047.
- Yokoo, Akihiko, & Ishihara, Kazuhiro. 2007. Analysis of pressure waves observed in Sakurajima eruption movies. *Earth Planets Space*, **59**(3), 177–181. doi:10.1186/BF03352691.
- Zhang, Guifang, Cai, Yixi, Zheng, Zhuo, Zhen, Junwei, Liu, Yongli, & Huang, Kangyou. 2016. Integration of the Statistical Index Method and the Analytic Hierarchy Process technique for the assessment of landslide susceptibility in Huizhou, China. *Catena*, **142**(jul), 233–244. doi:10.1016/J.CATENA.2016.03.028.